

Electron transverse transport enhancement by composite formation

Sang J. Park^{1,3,4}, Hojun Lee^{2,3}, Jongjun M. Lee², Jangwoo Ha¹, Hyun-Woo Lee^{2*} and Hyungyu Jin^{1,5*}

¹Department of Mechanical Engineering, Pohang University of Science and Technology (POSTECH), Pohang, 37673, South Korea.

²Department of Physics, Pohang University of Science and Technology (POSTECH), Pohang, 37673, South Korea.

³These authors contributed equally.

⁴Present address: National Institute for Materials Science, Tsukuba, 305-0047, Japan.

⁵Lead contact

*Correspondence: hgjin@postech.ac.kr (H.J.); hwl@postech.ac.kr (H.-W.L)

SUMMARY

Anomalous transverse transport of electrons such as the anomalous Hall effect and the anomalous Nernst effect provide opportunities to realize advanced spintronic and thermoelectric devices. To materialize these opportunities, it is crucial to strengthen the transverse transport. There have been considerable efforts to find new materials that fulfill this goal. Topological materials received a surge of recent attention in this regard. Here we report a different approach to enhance the transverse transport. Instead of searching for new materials, we propose mixing known materials to form composites. We show theoretically that randomly mixed arrays of two materials can exhibit significantly stronger transverse transport than the constituent materials. This enhancement is experimentally demonstrated for mixtures of crystallized and amorphous ferromagnetic metals. We identify the requirement of this enhancement, which can be satisfied by a wide class of materials. Thus, this scheme provides a universal method to strengthen transverse transport, together with rooms to accommodate various engineering requirements for device applications.

INTRODUCTION

Transverse transport (TT) in solids¹⁻⁶, where input and output electron fluxes are perpendicular to each other, allows various technological applications, including magnetic field sensors⁷, transverse thermoelectric generators⁸⁻¹⁷, and future spintronics devices¹⁸⁻²⁰. TT offers advantages to overcome the challenges of longitudinal transport. For example, TT allows to enhance the device output power by extending the extrinsic area perpendicular to input flux, eliminating the need for complex electrical contacts and multi-element structures commonly found in longitudinal devices^{8,9}. Furthermore, TT offers insights into the physical properties of solids²¹⁻²⁶, deepening our understanding of the complex interplay among charge, spin, and thermal fluxes.

The mechanisms of TT can be classified into intrinsic and extrinsic ones. The intrinsic mechanism^{27,28} utilizes the Berry phase, which is determined by energy eigenvalues and eigenstates of a pure material. On the other hand, extrinsic mechanisms (skew scattering mechanism²⁹ and side-jump mechanism³⁰) generate TT through electron scattering by disorders and phonons. The extrinsic contributions are usually smaller than the intrinsic contribution^{1,31}. Thus, efforts to strengthen TT have been focused on searching for exotic new materials with large intrinsic contribution. Topological materials are representative candidates of this sort and received great attention^{25,32-34}. Alternatively, the extrinsic skew scattering may be utilized to make TT larger than the intrinsic contribution, which is possible in super-clean materials³⁵ (materials with exceptionally low longitudinal resistivity). However, super-clean materials are difficult to realize in ambient conditions and thus unsuitable for device applications.

Our approach is different from the above. Our approach enhances the TT through the composite formation (Fig. 1A), which amounts to the *physical mixture* of two materials. It should be distinguished from the formation of *chemical* compounds with intermediate chemical composition. Our approach also differs from the aforementioned extrinsic mechanisms in that each constituent material forms domains of its own and maintains its TT, whereas the extrinsic mechanisms modify the TT of individual materials. The central idea of our approach is to form a multi-domain structure of two materials, where each domain is made of one of the two constituent materials. Intuitively, one may expect that the TT of the multi-domain structure is intermediate between those of the two constituent materials, as implied by the effective medium theory³⁶. Contrary to this expectation, we show theoretically that the multi-domain structure can exhibit stronger TT than the individual materials. The enhancement is particularly significant when one material with a relatively stronger TT than the other exhibits a relatively weaker longitudinal response than the other. Once this requirement of the material combination is satisfied, this enhancement scheme is applicable to any material combinations. We

demonstrate experimentally that this approach can enhance both the anomalous Hall effect (AHE) and the anomalous Nernst effect (ANE) to a level comparable to state-of-the-art single crystalline materials.

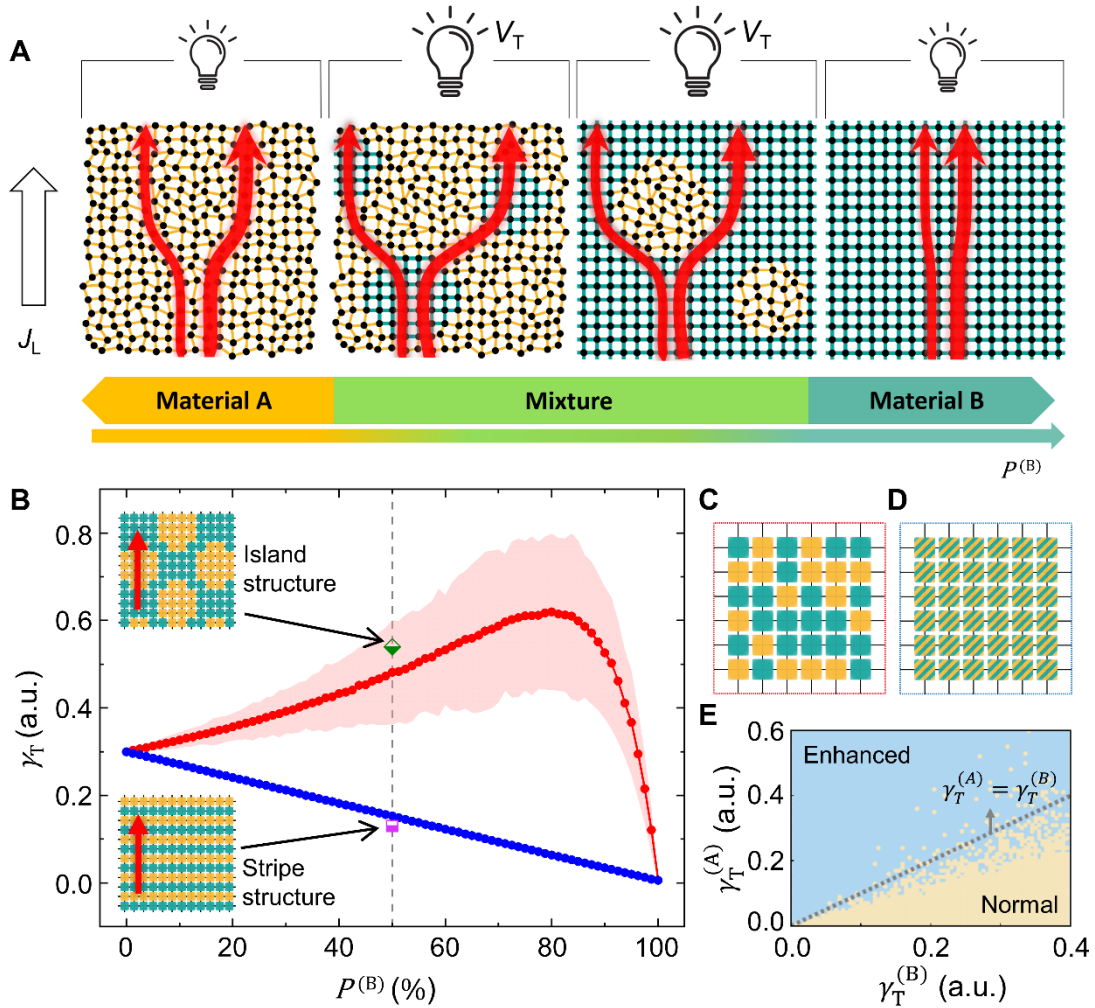


Fig. 1 | Enhancement of transverse transport (TT) in mixtures of two different materials. (A) Schematic of the physical mixture of material A (amorphous, yellow) and B (crystalline, cyan). J_L represents a longitudinal flux. When domains of A and B coexist, current paths (red arrows) become wiggly. (B) Transverse conductivity γ_T (red symbols and red area) of a random arrangement of A and B domains depicted in (C). The red symbols denote the average $\bar{\gamma}_T$ of γ_T over many random arrangements as a function of the portion of material B ($P^{(B)}$), whereas the red shaded area denotes 1.5- σ (standard deviation) range of γ_T . The blue symbols represent γ_T of the homogeneous network in (D) which consists of a single material with transport properties intermediate between the two materials A and B. The half-filled green diamond and purple square represent γ_T at $P^{(B)} = 50\%$ of the island and stripe structure networks, respectively, illustrated in the insets. The red arrows in the insets represents J_L . (E) Diagram showing the $\gamma_T^{(A)}$ and $\gamma_T^{(B)}$ dependence of the enhancement in $\bar{\gamma}_T$. A given combination $(\gamma_T^{(A)}, \gamma_T^{(B)})$ is marked sky blue if the enhancement of $\bar{\gamma}_T$ occurs, and beige if not.

RESULTS AND DISCUSSION

Theoretical model

We demonstrate our strategy by using a network model (Fig. 1C and Fig. S1, Note S1). Each site is occupied by either material A (lower longitudinal conductivity) with probability $P^{(A)}$ or material B (higher longitudinal conductivity) with probability $P^{(B)}$ ($P^{(A)} + P^{(B)} = 1$). To examine charge transport, for instance, the materials A and B at their respective sites are set to have longitudinal conductivities $\gamma_L^{(A)}$ and $\gamma_L^{(B)}$ ($\gamma_L^{(A)} < \gamma_L^{(B)}$) and transverse conductivities $\gamma_T^{(A)}$ and $\gamma_T^{(B)}$, respectively. A similar approach is possible for heat transport as well. Once the distributions of the materials A and B are fixed, the current profile and the voltage profile are fixed (see EXPERIMENTAL PROCEDURES and Notes S1-S3 in Supplemental Information for further details), allowing one to evaluate the longitudinal conductivity γ_L and the transverse conductivity γ_T of the network. For a given value of $P^{(B)}$, networks of the randomly arranged materials A and B are generated many times. For each realization of random arrangement, γ_L and γ_T are evaluated. Figure 1B shows the calculation result as a function of $P^{(B)}$. The red dots represent the average $\bar{\gamma}_T$ of γ_T over the realizations and the lightly-red-shaded area denotes the fluctuation range of γ_T . Interestingly, $\bar{\gamma}_T$ depends on $P^{(B)}$ in a nonmonotonic way. In particular, $\bar{\gamma}_T$ at an intermediate $P^{(B)}$ (in the case of Fig. 1B, $P^{(B)} = 80\%$) is higher than the values of $\bar{\gamma}_T$ at $P^{(B)} = 0\%$ and 100% . This shows that the mixture of two materials can have higher transverse conductivity than each pure material. To determine how generic the mixture-induced enhancement of $\bar{\gamma}_T$ is, we construct the $\bar{\gamma}_T$ vs $P^{(B)}$ diagram as a function of $\gamma_T^{(A)}$ and $\gamma_T^{(B)}$. Figure 1E shows its results: a given combination ($\gamma_T^{(A)}, \gamma_T^{(B)}$) is marked sky-blue if the diagram exhibits enhancement at intermediate $P^{(B)}$ and beige if not. Note that sky-blue dots almost completely fill the area in the region with $\gamma_T^{(A)} > \gamma_T^{(B)}$, indicating that the mixture-induced enhancement is quite generic for $\gamma_T^{(A)} > \gamma_T^{(B)}$.

To track down the origin of the enhancement, we consider a few specific networks and calculate their γ_T 's. First, we consider a homogeneous network (Fig. 1D), where all sites are occupied by the single material C with its transport properties intermediate between A and B: $\gamma_{L(T)}^{(C)} = P^{(A)}\gamma_{L(T)}^{(A)} + P^{(B)}\gamma_{L(T)}^{(B)}$. The blue dots in Fig. 1B show the resulting γ_T as a function of $P^{(B)}$. Note that the blue dots interpolate γ_T 's for $P^{(B)} = 0\%$ and 100% in a monotonic way, which follows the rule of mixtures. This result implies that for the *physical* mixture-induced enhancement (Fig. 1B, red dots) to occur, each site should keep the properties of either material A or B (instead of intermediate properties). That is, the mixture-induced enhancement originates from the physical mixture. Next, we consider the network, where

materials A and B form stripe structures (Fig. 1B, lower inset), and the network, where material A forms islands embedded in material B (Fig. 1B, upper inset). $P^{(B)}$ is set to 50% for both networks. γ_T for the stripe structure network is close to γ_T for the homogeneous network at $P^{(B)} = 50\%$, which indicates that the physical mixture alone does not guarantee the enhancement. On the other hand, γ_T for the island structure network is close to $\bar{\gamma}_T$ for the randomly generated inhomogeneously populated network (red dots). Thus, the mixture-induced enhancement occurs in the island structure network. To clarify the core difference between the stripe structure network and the island structure network, we calculate γ_T for additional structures and find that the enhancement occurs when the physical mixture makes charge current paths *wiggly*. In the island structure, for instance, the current paths tend to stay within the cyan region (region occupied by material B) and form wiggly paths simply because the longitudinal conductivity at each site is larger for domain B than domain A ($\gamma_L^{(A)} < \gamma_L^{(B)}$). Thus, the longitudinal conductance difference combined with the physical mixture generates trajectory “side-jump”s of island size (Fig. 1A, third panel, Fig. S2A to S2C, Note S2) even without the action of the transverse conductivities, $\gamma_T^{(A)}$ and $\gamma_T^{(B)}$. The role of $\gamma_T^{(A)}$ and $\gamma_T^{(B)}$ is to break the balance between left and right side-jump trajectories. In particular, the enhancement condition $\gamma_T^{(A)} > \gamma_T^{(B)}$ (Fig. 1e) implies that the balance breaking is caused near the sites where straight segments of the current paths encounter islands of material A. A similar enhancement occurs when materials A and B sites are swapped (Fig. 1A, second panel, Fig. S2D to S2F, Note S2). In this case, the current paths tend to minimize the portion in material A, which generates trajectory side-jumps. In the stripe structure network, in contrast, the physical mixture does not generate the trajectory side-jump, and thus the mixture-induced enhancement is not significant there. However, in randomly generated networks, networks similar to the stripe structure network are extremely unlikely and almost all networks have wiggly current paths, which indicates that the mixture-induced enhancement is quite generic if the condition $\gamma_T^{(A)} > \gamma_T^{(B)}$ is satisfied. In real materials formed by a physical mixture of materials A and B (e.g. composites), it is also highly likely that microstructures resembling the randomly generated networks are formed. Therefore, we put forward that the proposed strategy is applicable to a wide range of materials.

Experimental system: Ferromagnetic metallic glasses with controlled phase domains

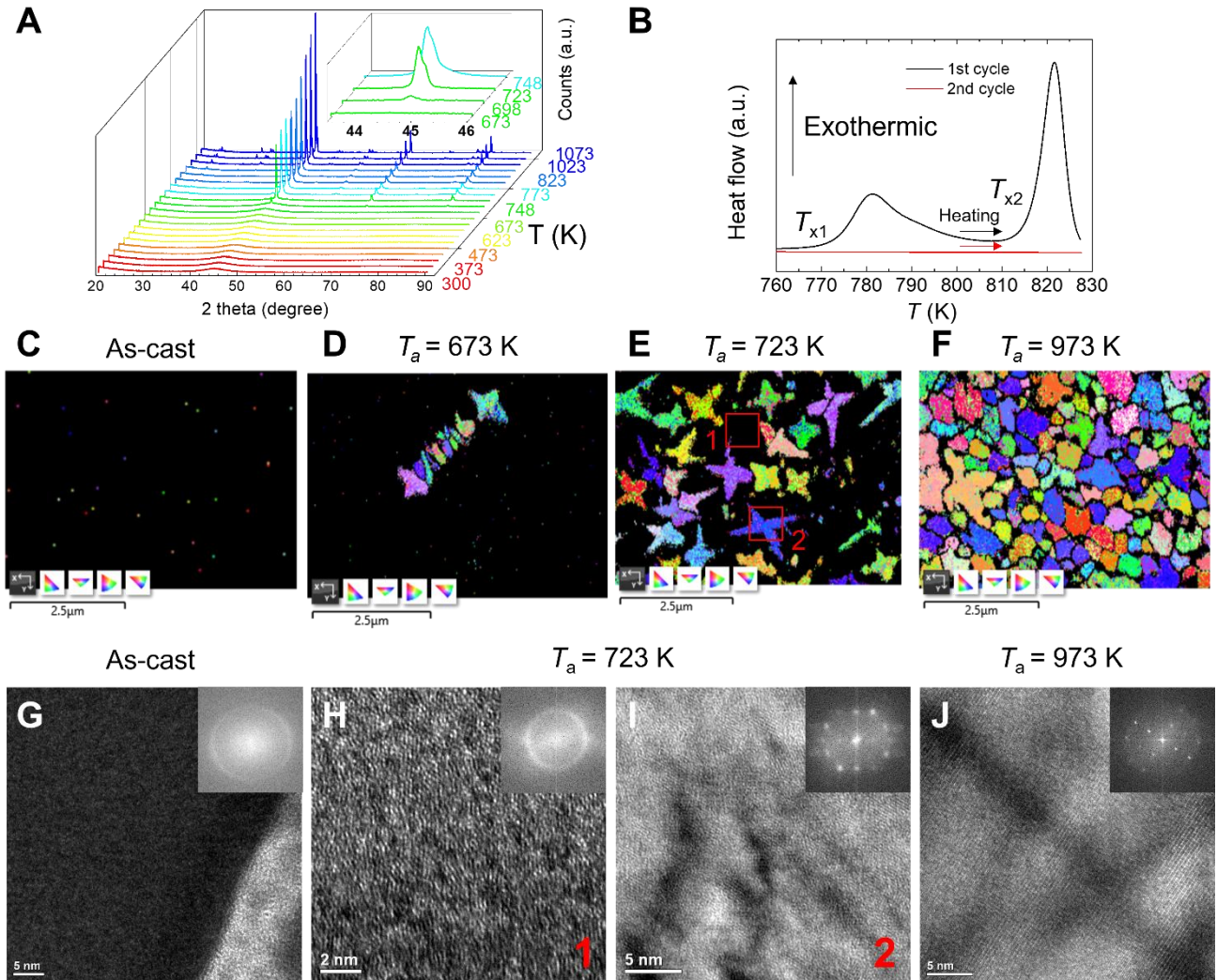


Fig. 2] Characterization of the amorphous and crystalline domains in Fe-based amorphous metals. (A) In-situ X-ray diffraction performed in the temperature range of 300–1073 K. The inset indicates the main peak around the crystallization temperature of approximately 700 K. (B) Differential scanning calorimetry with two-step exothermic reactions for crystallizations at T_{x1} and T_{x2} . No peak is observed in the consecutive second cycle, confirming the irreversibility of the reactions. Both cycles were conducted while increasing the temperature at a rate of 5 K/min (EXPERIMENTAL PROCEDURES). (C to F) Color mapping images of crystalline phases measured using scanning electron microscopy equipped with an electron back-scattered diffraction module in as-cast (C), $T_a=673$ K (D), $T_a=723$ K (E), and $T_a=973$ K samples (F). (G to J) Transmission electron microscopy images of amorphous (as-cast, G), partially crystallized ($T_a=723$ K, h and i), and poly-crystalline ($T_a=973$ K, J) samples. The insets in (G to J) indicate the diffraction patterns obtained using the fast Fourier transform. (H and I) were obtained at amorphous and crystalline spots in the same $T_a = 723$ K sample, given in (E).

We now introduce the experimental system for the test of the theoretical prediction. We chose ferromagnetic metallic glasses of composition $\text{Fe}_{92.5}\text{Si}_5\text{B}_{2.5}$ as the test system, where the proportion of heterostructures (i.e., crystalline phase vs. amorphous phase) can be systematically adjusted by varying

the annealing temperature T_a (Fig. 2). The two phases may be regarded as two different materials for our purpose. The amorphous phase has lower longitudinal (higher transverse) conductivity than the crystalline phase, as confirmed in Fig. 3C (3D). A composite that consists of domains of the two phases can render a system that satisfies the predicted requirement for the enhancement. Two sets of samples were prepared for validation with two different annealing times: 1 h and 5 min. While both sets clearly demonstrated the validity of the model, we focus on the 1-h annealed set in the main text, which shows clearer crystalline-amorphous domain distributions without the formation of metastable phases. Therefore, the presented data in the following sections correspond to the 1-h annealed set, unless otherwise noted. The TT data from the 5-min annealed set are provided in Supplemental Information.

The domain distribution was first assessed using in-situ X-ray diffraction (XRD) on the as-cast sample, increasing temperature from 300 to 1073 K (Fig. 2A and EXPERIMENTAL PROCEDURES for details). The crystallization onset was identified at 723 K, beyond which distinct crystalline peaks emerged. Further in-situ XRD analysis during cooling from 1073 K back to 300 K confirmed the persistence of these crystalline peaks at low temperatures, indicating irreversibility of the crystallization (Fig. S3). Differential scanning calorimetry (DSC) characterized the dynamic structural transition (Fig. 2B), revealing two distinct exothermic peaks at $T_{x1}=780$ K and $T_{x2}=820$ K, characteristic of crystallization^{37,38}. The absence of transition peaks during the second DSC cycle also supports the irreversible nature of the observed exothermic reactions.

To systematically explore the influence of domain distribution on TT, we selected five representative T_a of 673, 698, 723, 773, and 973 K with an unannealed (as-cast) sample for reference (EXPERIMENTAL PROCEDURES). Electron backscattered diffraction (EBSD) imaging revealed an increase in the crystalline fraction with rising T_a (Figs. 2C to 2F). In the $T_a=673$ K sample, multiphase grain islands began crystallizing, evolving predominantly into dendritic structures with increasing T_a ^{39,40}. The $T_a=973$ K sample was observed to be nearly fully crystallized, albeit retaining a minor amorphous fraction. The evolution of sample morphology with varying T_a was further corroborated using transmission electron microscopy (TEM) (Figs. 2G to 2J). Low-magnification TEM images of the $T_a=723$ K sample distinctly showed dendritic structures (Fig. S4). Selected area diffraction patterns, obtained through the fast Fourier Transform, indicated a gradual transition from amorphous (as-cast) to crystalline ($T_a=973$ K). We find that the $T_a=723$ K sample exhibits a heterostructure that resembles the island structure network in our theoretical model (Fig. 1N, inset). Overall, we confirm that the intended sample set is successfully constructed, wherein the ratio between amorphous and crystalline domains is systematically varied with T_a .

Experimental validation of network model via transport measurements

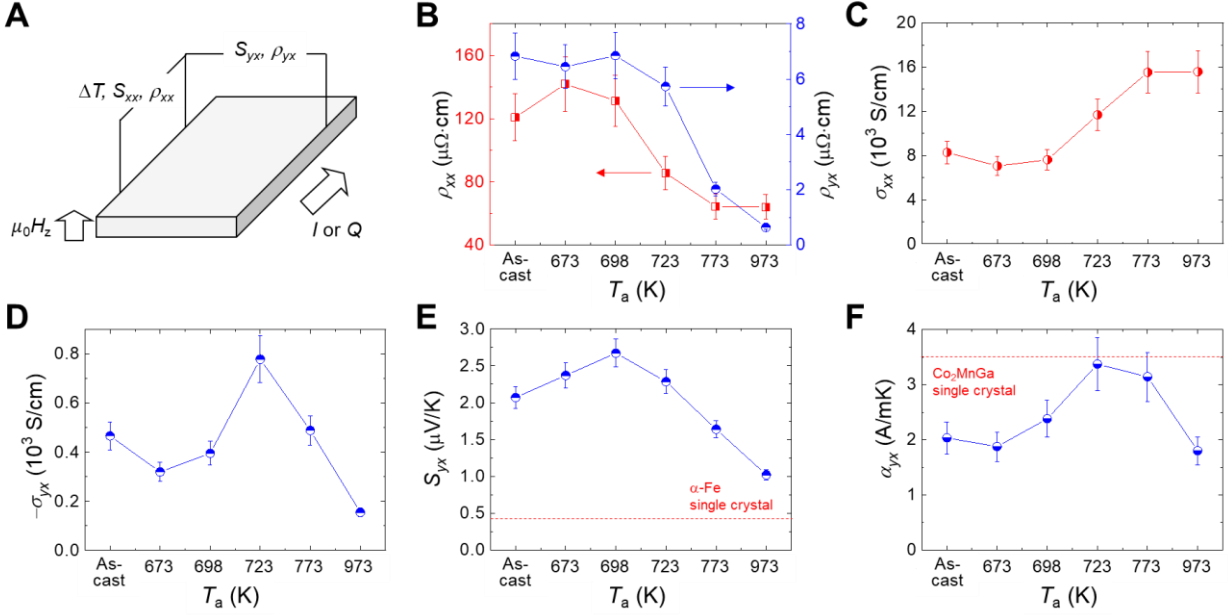


Fig. 3] Experimental demonstration of enhanced transverse transport (TT) in hetero-composites. (A) Measurement schematic of transport properties in response to longitudinal electrical (I) and thermal (Q) fluxes. Measurement details can be found in EXPERIMENTAL PROCEDURES and Fig. S5. (B) Longitudinal electrical resistivity (ρ_{xx}) and anomalous Hall resistivity (ρ_{yx}) as a function of annealing temperature (T_a). (C) Longitudinal electrical conductivity (σ_{xx}) and (D) anomalous Hall conductivity (σ_{yx}). (E) Anomalous Nernst coefficient (S_{yx}) and (F) anomalous Nernst conductivity (α_{yx}). All properties in (B) to (F) were measured at $T=300$ K. Temperature-dependent properties can be found in Fig. S6 in Supplementary Materials. The error bars were estimated based on the standard deviation of measurements.

We now present experimental evidence of enhanced TT in random physical mixtures of amorphous and crystalline domains that supports our theoretical network model (Fig. 3, see EXPERIMENTAL PROCEDURES for measurement details). Figures 3C and 3D show that the amorphous as-cast sample possesses a lower longitudinal electrical conductivity ($\sigma_{xx}=8.28\times 10^3$ S/cm at $T=300$ K) and a higher transverse anomalous Hall conductivity ($|\sigma_{yx}|=467$ S/cm where $\sigma_{yx} = -\frac{\rho_{yx}}{\rho_{xx}^2 + \rho_{yy}^2}$) compared to its crystalline counterpart ($\sigma_{xx}=15.6\times 10^3$ S/cm and $|\sigma_{yx}|=155$ S/cm for $T_a=973$ K). Here, x and y represent the directions of applied charge (I) or heat current (Q) and measured transverse voltage, respectively, following the sign convention in ref.¹³ (Fig. 3A and Fig. S5). We note that this satisfies the condition for the occurrence of enhanced TT in our network model. As a result, the enhanced TT is clearly observed in the samples with island-like heterostructures at 300 K (Fig. 3D) with T -dependence provided in Fig. S6 (Note S3); σ_{yx} peaks at $T_a=723$ K ($|\sigma_{yx}|=780$ S/cm at $T=300$ K), significantly exceeding the values for both amorphous (i.e., as-cast) and crystalline (i.e., $T_a=973$ K) samples. The non-monotonic dependence of σ_{yx} on T_a contrasts with the near monotonic dependence of σ_{xx} , revealing the more sensitive nature of TT to the microscopic domain distribution than its longitudinal counterpart.

Notably, $|\sigma_{yx}|=780$ S/cm for the $T_a=723$ K sample corresponds to as much as ~ 5 -fold enhancement compared to that for the crystalline ($T_a=973$ K) sample. Such strong enhancement leads to an impressive anomalous Hall angle (AHA= $\left|\frac{\sigma_{yx}}{\sigma_{xx}}\right|\times 100\%$) of 6.7%, which is even larger than those of Fe-based single crystalline Fe₃Ga and Fe₃Al ($|\sigma_{yx}|=440\text{--}540$ S/cm and AHA=3.7–5.1% at $T=300$ K)¹¹, despite the much smaller amount of secondary elements used in our materials (Fe_{92.5}Si₅B_{2.5}). Note that before the enhancement, the AHA of our crystalline ($T_a=973$ K) sample is merely 0.99%.

Enhanced TT is also consistently observed in the thermal transport represented by ANE at 300 K (See Figs. S6 and S7 and Note S4 for T -dependent data and thermal conductivity of 1-h annealed set, respectively, and Fig. S8 for 5-min annealed set). The anomalous Nernst coefficient (S_{yx}) shows a similar behavior with σ_{yx} , where the heterostructure samples outperform their amorphous and crystalline counterparts (Fig. 3E and Fig. S8A). S_{yx} increases with T_a within the sample set annealed for 1 h (5 min), reaching 2.67 $\mu\text{V/K}$ (3.69 $\mu\text{V/K}$) for the heterostructure sample with $T_a=698$ K ($T_a=773$ K) before diminishing to 0.97 $\mu\text{V/K}$ for the $T_a=973$ K crystalline sample. The enhanced S_{yx} values in the heterostructure samples are one order higher than that of α -Fe single crystals (~ 0.3 $\mu\text{V/K}$). Considering the composition of our samples is Fe_{92.5}Si₅B_{2.5}, where Fe is the major constituent element, it is remarkable that the manipulation of domain structure with a small fraction of Si and B substitution can lead to such a significant enhancement in S_{yx} . We also evaluated the anomalous Nernst conductivity ($\alpha_{yx} = S_{xx}\sigma_{yx} + S_{yx}\sigma_{xx}$), a pivotal TT parameter that directly connects longitudinal temperature gradient with transverse electric current (Fig. 3F and Fig. S8B)^{41–43}. The largest value of 3.37 A/(m·K) (4.94 A/(m·K)) is shown by the $T_a=723$ K ($T_a=773$ K) heterostructure sample annealed for 1 h (5 min), which corresponds approximately to double (triple) that of the $T_a=973$ K crystalline sample (1.72 A/(m·K)). The observed α_{yx} values are comparable and even larger than those of state-of-the-art single crystals such as Co₂MnGa (3–3.4 A/(m·K))^{12,44,45} and Fe₃Ga (4.49–4.83 A/(m·K))¹¹, whose large α_{yx} values are attributed to intrinsic band topology.

In addition to the enhancement of various TT coefficients, the peak location of $T_a=723$ K (or 698 K) also supports our theoretical prediction. According to our theoretical model, the TT is enhanced in the parameter range (T_a is the relevant parameter in our experimental situation) where straight current paths are suppressed and replaced by wiggly paths (2nd and 3rd panels in Fig. 1A). In our experiment, σ_{xx} changes rapidly near $T_a=723$ K from its crystalline value to the amorphous value, and thus wiggly paths should be most pronounced near $T_a=723$ K, which is the location where TT is enhanced in agreement with the theoretical prediction. This observation is consistent with the microscopic structure

observation where the $T_a=723$ K sample shows the distinct island-like crystalline phase domains in the amorphous matrix (Fig. 2E). We further investigate whether the strong enhancement of σ_{yx} , S_{yx} , and α_{yx} in our heterostructure samples can be explained by other mechanisms. We specifically consider the case of σ_{yx} which has been extensively studied over past decades^{1,35,42}. When the intrinsic Berry curvature mechanism is the dominant source of σ_{yx} , σ_{yx} should be independent of σ_{xx} ⁴⁶. On the other hand, when the extrinsic mechanisms such as the skew scattering mechanism⁴⁷ or the side jump mechanism³⁰ is the dominant source of σ_{yx} , σ_{yx} should be proportional to σ_{xx} or independent of σ_{xx} , respectively. Comparison between experimental σ_{xx} and σ_{yx} (Figs. 3C and 3D) indicates that neither of the relations is satisfied, implying that the enhancement of TT in our experiment is not due to the conventional mechanisms (additional information in Notes S5 and S6, and Figs. S9-S13). In contrast, our theoretical model naturally explains the peak formation of σ_{yx} in the region where σ_{xx} changes rapidly. We thus believe that our mechanism provides a convincing explanation for the observed σ_{yx} enhancement in our heterostructure samples, wherein amorphous and crystalline phases (as if they are two different materials) are physically mixed.

Overall, the experimental results strongly support the theoretical prediction of the network model. The clear dependency of AHE and ANE on T_a and the corresponding microscopic structure suggests that the dominant source responsible for the enhancement is the formation of island-like domains, which leads to wiggly current paths. A recent experiment reported that nanostructure engineering can mysteriously enhance the transverse thermoelectric conversion⁴⁸. Since the nanostructure engineering leads to the composite formation similar to our experimental system, we argue that our mechanism provides an explanation to the reported enhancement. Such consistent observations in different material systems corroborate the universal applicability of our enhancement scheme across broad material classes and their combinations.

CONCLUSIONS

The universality of the proposed approach for enhancing TT essentially arises from its independence from specific material parameters in our theoretical model, such as crystallographic orientation and electronic band structure. The approach in principle can be applied to any physical mixtures of two materials that satisfy the following requirements: 1) satisfying inequalities in the longitudinal and transverse conductivities between material A and B (i.e., $\gamma_L^{(A)} < \gamma_L^{(B)}$ and $\gamma_T^{(A)} > \gamma_T^{(B)}$), and 2) forming hetero-domains that give rise to wiggly current paths. This allows the creation of new materials with large TT by mixing already existing materials. When this enhancement scheme is applied to a combination that includes state-of-the-art materials, there is a possibility to go even beyond the state-of-the-art TT. Furthermore, occasional discoveries of new material classes will provide opportunities to create new large TT materials using the proposed approach. Thus, the impact of our work is likely to be perpetual in relevant research fields that utilize the transverse transport of electrons in solids.

While we exemplified our approach with the well-known anomalous Hall and Nernst effects in electronic systems, we expect that our approach can be applied to enhance the transverse transport of various kinds of flux. For example, it may be applied to the transverse transport of an ionic flux, such as the ionic Hall effect in heterogeneous composites consisting of ionic conductors. Therefore, our approach may contribute to developing novel device applications based on transverse transport of different kinds of flux. Lastly, the materials created by the proposed approach will be non-single crystalline, which offers practical advantages over single crystalline materials such as better mechanical stability and lower fabrication cost.

EXPERIMENTAL PROCEDURES

2D network model. The two-dimensional square network is constructed with cross (+) junctions. Each junction is connected with four wires, on which the voltage $V_{1,2,3,4}$ and the current $I_{1,2,3,4}$ are assigned (Fig. S1A). We assume that the steady current flows in the wires and the transport properties of each + junction are completely described by the conductance tensor G_{ij} . We assume the linear response theory, in which the current I_i flowing into the i th wire is related to the voltage V_j applied to the j th wire by $I_i = \sum_j G_{ij} V_j$. Under the charge conservation and the gauge invariance of the current, the conductance tensor should satisfy $\sum_j G_{ij} = \sum_j G_{ij} = 0$. Since we deal with the situation where TT occurs, we assume that the time-reversal symmetry is broken in this system. By the C_{4z} symmetry and the above relations, G_{ii} can be determined by three independent parameters G_S , c , and G_A as follows

$$G_{ij} = \frac{1}{2} [(3\delta_{i,j} + \delta_{i,j-2} - 1) + c(3\delta_{i,j-2} + \delta_{i,j} - 1)] G_S + \frac{1}{2} (\delta_{i,j-1} - \delta_{i,j-3}) G_A$$

The parameter G_A is asymmetric under the time-reversal symmetry so that it characterizes the TT (Fig. S1B), while G_S and c are symmetric. Similar discussions for the honeycomb lattice can be found in previous studies^{49,50}.

The transport of the whole network system is determined by the G_{ij} of each junction and boundary conditions. We take a finite $N_x \times N_y$ square network with four edges. Thus, the network is described by the linear equation $\mathbf{I} = \mathbf{G}\mathbf{V}$ with constraints, where $\mathbf{G} = \bigoplus_{i=1}^N G^{(i)}$, $\mathbf{I} = (I^{(1)}, I^{(2)}, \dots, I^{(N)})^T$, and $\mathbf{V} = (V^{(1)}, V^{(2)}, \dots, V^{(N)})^T$. Here, \bigoplus denotes the direct sum of the 4×4 matrices $G^{(i)}$, and $N = N_x N_y$. The results of Fig. 1B in the main text was obtained for $N_x = N_y = 40$. The junction parameters were set to $G_S^A = 5$, $c^A = -0.8$, $G_A^A = 0.6$, $G_S^B = 100$, $c^B = -0.9$, and $G_A^B = 0.01$, where the superscripts A(B) denotes the domain A(B), respectively. The boundary condition was set on the four edges. The currents passing through the left and the right edges of the system were fixed to be zero. The currents injected to the bottom edge and the currents extracted from the top edge were set to be uniform. Next, we introduced the constraints $V_i^{(n)} = V_j^{(m)}$ and $I_i^{(n)} = -I_j^{(m)}$ to reduce the dimension of the problem, where i th wire of n th junction and j th wire of m th junction are connected to each other. Finally, we fixed the gauge by setting an arbitrary potential to be zero. Then, we performed a numerical calculation to solve this reduced linear equation and obtained the voltages on the edges. In order to simulate the values measured in actual experiments, we repeated the calculation for the opposite direction of the magnetization or magnetic field and corrected the voltage. The transverse conductivity γ_T of the whole system was calculated from these voltages and the input current. To obtain $\bar{\gamma}_T$ of the random network

in Fig. 1B in the main text (red points), we averaged γ_T for 100 randomly generated domain formations for a given $P^{(B)}$.

The result of Fig. 1E in the main text is obtained for a square network with $N_x = N_y = 20$. The junction parameters were set to be the same as those of the square network for Fig. 1B in the main text, except for G_A^A and G_A^B . Note that $\gamma_T^{(A)}$ or $\gamma_T^{(B)}$ is directly determined by G_A^A or G_A^B , respectively, unlike the mixed case. To determine whether the mixture-induced enhancement occurs at each point of the diagram, we selected 15 values of portion $P^{(B)}$ at equal intervals and calculated $\bar{\gamma}_T$ for each $P^{(B)}$. To focus on the effect of the junction parameters, we repeated the calculations for the same $P^{(B)}$ and found 0.2- σ interval from its average value. We determined that the enhancement occurred if there existed a portion $P^{(B)}$ at which the infimum of its interval was larger than both γ_T of end values of $P^{(B)}$.

Preparation of domain-controlled heterostructure samples. Domain-controlled samples were prepared by annealing an Fe-based amorphous metal, specifically Metglas (2605 SA1 for main data, Proterial), in an inert atmosphere at various temperatures. The amorphous metals were cut into pieces of approximately 3 mm \times 6 mm and loaded into quartz ampoules. To prevent oxidation, the ampoules were sealed under a partial 6N Ar atmosphere. Two sets of samples were prepared with two different annealing times of 1 h and 5 min. The 1-h annealed samples were heated in a furnace at a ramp rate of 5 K/min and maintained for 1 h at temperatures of 673, 698, 723, 773, and 973 K, respectively. The 5-min annealed samples were heated in a furnace at a ramp rate of 10 K/min and maintained for 5 min at temperatures of 623, 673, 723, and 823 K, respectively. Finally, the 1-h annealed samples were naturally cooled in the furnace, while the 5-min annealed samples were water quenched.

Characterization of the structural disorder using XRD. The crystallinity and structural disorder of the amorphous samples were characterized using in-situ XRD (EMPYREAN, Marlvern Panalytical) with Cu K α radiation at 45 kV and 40 mA. The theta-2theta scan was performed after a 10-min hold at each temperature using a 255-channel strip detector (PIXcel^{1D}, Marlvern Panalytical) to minimize the dynamic change in crystallinity during the scan. The ramp rate was set at 5 K/min. The atmosphere for the in-situ measurements was filled with inert N₂ gas at a flow rate of 50 cc/min. Ex-situ XRD measurements (D/MAX-2500/PC, Rigaku) were conducted on pre-annealed samples at room temperature in the air with Cu K α at 40 kV and 100 mA.

Imaging the microstructure and local disorder. The microstructures of the samples were characterized using a scanning electron microscope (JSM-IT800HL, JEOL) combined with an EBSD detector (C-Nano, Oxford) at an acceleration voltage of 15 kV. Atomic-scale crystallinity was

investigated using high-resolution TEM (JEM-2100F, JEOL) at an acceleration voltage of 200 kV. The TEM images were analyzed using Gatan software.

Differential scanning calorimeter. The exothermic reactions for recrystallization were investigated using DSC (DSC 200 F3 Maia, Netzsch) following the ASTM E-1269 standard. The temperature was increased from 300 K to 823 K at a heating rate of 5 K/min. The atmosphere was maintained at 5 N with N₂ gas during the measurements.

Measurement of transport properties. Electrical and thermal properties were measured using a cryogen-free measurement system (CFMS, Cryogenics). The electrical and Hall resistances were measured using an AC resistance bridge (Model 372, Lake Shore Cryogenics) with a current density of approximately 5×10^4 A/m². The thermal conductivity and Seebeck and Nernst effects were measured using an in-plane configuration incorporating two Peltier devices (NL 1010T-01AC, Marlow Industries) and two T-type thermocouples (Fig. S5 for details). A Peltier device was employed to pump heat into the sample using the Peltier effect with an electrical current of 100–150 mA supplied by a current source (E3646A, Agilent), whereas the other served as a heat flux sensor, measuring the heat flux using pre-calibrated heat flux sensitivity data for each temperature. Thermal grease (N & H grease, Apiezon) and GE varnish (GE 7031, CMR direct) were used between the cryostat stage, Peltier devices, and samples to reduce thermal contact resistances and ensure uniform temperature distribution across the sample. The thermocouples were attached using silver epoxy (H20E, EPO-TEK) to measure the TE voltages (2182A, Keithley). All measurements utilized 25.4-diameter wires (SPCP- and SPCI-001-50, Omega Engineering) and were conducted under a high-vacuum condition ($<10^{-5}$ Torr) to minimize heat losses by conduction and convection.

Measurement of magnetic properties. Magnetic properties were measured using a SQUID-VSM (MPMS 3, Quantum Design) with a high-temperature oven option. The temperature was increased from 300 K to 760 K at a ramp rate of 5 K/min.

Simulation of Seebeck-driven transverse thermoelectric generation (STTG). The contribution of STTG to the enhanced S_{yx} was investigated using a thermoelectric module in COMSOL Multiphysics software, combining Fourier's law, Ohm's law, and thermoelectric effects. A simplified composite model was introduced, assuming spherical crystalline structures embedded in an amorphous host (Fig. S13, Note S6). The TT was considered by including off-diagonal terms (e.g., ρ_{xy} , and S_{xy}) in the conductivity and thermopower tensors⁵¹. The interfacial electrical and thermal contact resistances were neglected.

RESOURCE AVAILABILITY

Lead contact

Correspondence and requests for materials and data should be addressed to the lead contact, Hyungyu

Jin (hgjin@postech.ac.kr)

Materials availability

This study did not generate new unique reagents.

Data and code availability

The supplemental information is available in the online version of the paper.

ACKNOWLEDGEMENTS

The authors thank Proterial Korea, Ltd. for providing the commercial amorphous metals (2605SA1) for research purposes. The authors thank Ki Mun Bang for help with figures and Ji-Hyun Seong, Ho-Jun Gang, Jung-Hun Kim, and Eun-Ho Lee for their technical support.

This work was supported by Samsung Research Funding & Incubation Center of Samsung Electronics under Project Number SRFC-MA2002-02, National Research Foundation of Korea (NRF) grant funded by the Korea government (MSIT) RS-2024-00345022 and No. NRF-2022M3C1A3091988, Samsung Science and Technology Foundation grant BA-1501-51, National Research Foundation of Korea (NRF) grant funded by the Korean government (MSIT) RS-2024-00410027, and National Supercomputing Center with supercomputing resources including technical support (KSC-2022-CRE-0468).

AUTHOR CONTRIBUTIONS

Sang J. Park: Conceptualization, Data curation, Forman analysis, Investigation, Methodology, Validation, Visualization, Writing – original draft, Writing – review & editing. **Hojun Lee:** Data curation, Forman analysis, Investigation, Methodology, Software, Validation, Visualization, Writing – original draft, Writing – review & editing. **Jongjun M. Lee:** Data curation, Forman analysis, Investigation, Methodology, Software, Validation, Visualization, Writing – review & editing. **Jangwoo Ha:** Data curation, Forman analysis, Investigation, Methodology, Software, Visualization. **Hyun-Woo Lee:** Funding acquisition, Investigation, Methodology, Project administration, Supervision, Validation, Writing – review & editing. **Hyungyu Jin:** Conceptualization, Funding acquisition, Investigation, Methodology, Project administration, Supervision, Validation, Writing – review & editing.

DECLARATION OF INTERESTS

The authors declare no competing interests.

SUPPLEMENTAL INFORMATION

Supplemental information can be found online at .

References

1. Nagaosa, N., Sinova, J., Onoda, S., MacDonald, A.H., and Ong, N.P. (2010). Anomalous Hall effect. *Rev Mod Phys* 82, 1539–1592. <https://doi.org/10.1103/RevModPhys.82.1539>.
2. Sinova, J., Valenzuela, S.O., Wunderlich, J., Back, C.H., and Jungwirth, T. (2015). Spin Hall effects. *Rev Mod Phys* 87, 1213–1260. <https://doi.org/10.1103/RevModPhys.87.1213>.
3. von Klitzing, K., Chakraborty, T., Kim, P., Madhavan, V., Dai, X., McIver, J., Tokura, Y., Savary, L., Smirnova, D., Rey, A.M., et al. (2020). 40 years of the quantum Hall effect. *Nature Reviews Physics* 2, 397–401. <https://doi.org/10.1038/s42254-020-0209-1>.
4. Chang, C.Z., Liu, C.X., and Macdonald, A.H. (2023). Colloquium: Quantum anomalous Hall effect. *Rev Mod Phys* 95, 011002. <https://doi.org/10.1103/RevModPhys.95.011002>.
5. Bauer, G.E.W., Saitoh, E., and Van Wees, B.J. (2012). Spin caloritronics. *Nat Mater* 11, 391–399. <https://doi.org/10.1038/nmat3301>.
6. Boona, S.R., Myers, R.C., and Heremans, J.P. (2014). Spin caloritronics. *Energy Environ Sci* 7, 885–910. <https://doi.org/10.1039/c3ee43299h>.
7. Tumanski, S. (2013). Modern magnetic field sensors – a review. *Przeglad Elektrotechniczny* 89, 1–12.
8. Uchida, K., and Heremans, J.P. (2022). Thermoelectrics: From longitudinal to transverse. *Joule* 6, 2240–2245. <https://doi.org/10.1016/j.joule.2022.08.016>.
9. Boona, S.R., Jin, H., and Watzman, S. (2021). Transverse thermal energy conversion using spin and topological structures. *J Appl Phys* 130, 171101. <https://doi.org/10.1063/5.0062559>.
10. Ikhlās, M., Tomita, T., Koretsune, T., Suzuki, M.T., Nishio-Hamane, D., Arita, R., Otani, Y., and Nakatsuji, S. (2017). Large anomalous Nernst effect at room temperature in a chiral antiferromagnet. *Nat Phys* 13, 1085–1090. <https://doi.org/10.1038/nphys4181>.
11. Sakai, A., Minami, S., Koretsune, T., Chen, T., Higo, T., Wang, Y., Nomoto, T., Hirayama, M., Miwa, S., Nishio-Hamane, D., et al. (2020). Iron-based binary ferromagnets for transverse thermoelectric conversion. *Nature* 581, 53–57. <https://doi.org/10.1038/s41586-020-2230-z>.
12. Sakai, A., Mizuta, Y.P., Nugroho, A.A., Sihombing, R., Koretsune, T., Suzuki, M.T., Takemori, N., Ishii, R., Nishio-Hamane, D., Arita, R., et al. (2018). Giant anomalous Nernst effect and quantum-critical scaling in a ferromagnetic semimetal. *Nat Phys* 14, 1119–1124. <https://doi.org/10.1038/s41567-018-0225-6>.
13. Pan, Y., Le, C., He, B., Watzman, S.J., Yao, M., Gooth, J., Heremans, J.P., Sun, Y., and Felser, C. (2022). Giant anomalous Nernst signal in the antiferromagnet YbMnBi₂. *Nat Mater* 21, 203–209. <https://doi.org/10.1038/s41563-021-01149-2>.
14. He, B., Şahin, C., Boona, S.R., Sales, B.C., Pan, Y., Felser, C., Flatté, M.E., and Heremans, J.P. (2021). Large magnon-induced anomalous Nernst conductivity in single-crystal MnBi. *Joule* 5, 3057–3067. <https://doi.org/10.1016/j.joule.2021.08.007>.
15. Fu, C., Guin, S.N., Watzman, S.J., Li, G., Liu, E., Kumar, N., Süb, V., Schnelle, W., Auffermann, G., Shekhar, C., et al. (2018). Large Nernst power factor over a broad temperature range in polycrystalline Weyl semimetal NbP. *Energy Environ Sci* 11, 2813–2820. <https://doi.org/10.1039/c8ee02077a>.
16. Guin, S.N., Vir, P., Zhang, Y., Kumar, N., Watzman, S.J., Fu, C., Liu, E., Manna, K., Schnelle, W., Gooth, J., et al. (2019). Zero-Field Nernst Effect in a Ferromagnetic Kagome-Lattice Weyl-Semimetal Co₃Sn₂S₂. *Advanced Materials* 31, 1806622. <https://doi.org/10.1002/adma.201806622>.
17. Zhou, W., Yamamoto, K., Miura, A., Iguchi, R., Miura, Y., Uchida, K., and Sakuraba, Y. (2021). Seebeck-driven transverse thermoelectric generation. *Nat Mater* 20, 463–467. <https://doi.org/10.1038/s41563-020-00884-2>.
18. Hirohata, A., Yamada, K., Nakatani, Y., Prejbeanu, L., Diény, B., Pirro, P., and Hillebrands, B. (2020). Review on spintronics: Principles and device applications. *J Magn Magn Mater* 509, 166711. <https://doi.org/10.1016/J.JMMM.2020.166711>.
19. Diény, B., Prejbeanu, I.L., Garello, K., Gambardella, P., Freitas, P., Lehdorff, R., Raberg, W., Ebels, U., Demokritov, S.O., Akerman, J., et al. (2020). Opportunities and challenges for spintronics in the microelectronics industry. Preprint at Nature Research, <https://doi.org/10.1038/s41928-020-0461-5> <https://doi.org/10.1038/s41928-020-0461-5>.
20. Park, S.J., Cao Van, P., Kang, M.-G., Jung, H.-J., Kim, G.-Y., Choi, S.-Y., Yoo, J.-W., Park, B.-G., Kim, S.K., Jeong, J.-R., et al. (2024). Enhancing spin pumping by nonlocal manipulation of magnon temperature. *Matter* 7, 4332–4341. <https://doi.org/10.1016/j.matt.2024.08.023>.
21. Fu, L., and Kane, C.L. (2007). Topological insulators with inversion symmetry. *Phys Rev B Condens Matter Mater Phys* 76, 045302. <https://doi.org/10.1103/PHYSREVB.76.045302/FIGURES/7/MEDIUM>.
22. Zhang, L., Ren, J., Wang, J.S., and Li, B. (2010). Topological nature of the phonon Hall effect. *Phys Rev Lett* 105, 225901. <https://doi.org/10.1103/PHYSREVLTT.105.225901/FIGURES/2/MEDIUM>.
23. Cai, J., Anderson, E., Wang, C., Zhang, X., Liu, X., Holtzmann, W., Zhang, Y., Fan, F., Taniguchi, T., Watanabe, K., et al. (2023). Signatures of fractional quantum anomalous Hall states in twisted MoTe₂. *Nature* 622, 63–68. <https://doi.org/10.1038/s41586-023-06289-w>.

24. Onose, Y., Ideue, T., Katsura, H., Shiomi, Y., Nagaosa, N., and Tokura, Y. (2010). Observation of the magnon Hall effect. *Science* (1979) *329*, 297–299. <https://doi.org/10.1126/science.1188260>.
25. Kane, C.L., and Mele, E.J. (2005). Z₂ topological order and the quantum spin Hall effect. *Phys Rev Lett* *95*, 146802. <https://doi.org/10.1103/PhysRevLett.95.146802>.
26. Katsura, H., Nagaosa, N., and Lee, P.A. (2010). Theory of the thermal Hall effect in quantum magnets. *Phys Rev Lett* *104*, 066403. <https://doi.org/10.1103/PhysRevLett.104.066403>.
27. Karplus, R., and Luttinger, J.M. (1954). Hall Effect in Ferromagnetics. *Physical Review* *95*, 1154. <https://doi.org/10.1103/PhysRev.95.1154>.
28. Jungwirth, T., Niu, Q., and MacDonald, A.H. (2002). Anomalous Hall Effect in Ferromagnetic Semiconductors. *Phys Rev Lett* *88*, 207208. <https://doi.org/10.1103/PhysRevLett.88.207208>.
29. Smit, J. (1958). The spontaneous hall effect in ferromagnetics II. *Physica* *24*, 39–51. [https://doi.org/10.1016/S0031-8914\(58\)93541-9](https://doi.org/10.1016/S0031-8914(58)93541-9).
30. Berger, L. (1970). Side-Jump Mechanism for the Hall Effect of Ferromagnets. *Physics Review B* *2*, 4559–4566.
31. Xiao, D., Chang, M.C., and Niu, Q. (2010). Berry phase effects on electronic properties. *Rev Mod Phys* *82*, 1959–2007. <https://doi.org/10.1103/REVMODPHYS.82.1959/FIGURES/16/MEDIUM>.
32. Haldane, F.D.M. (2004). Berry Curvature on the Fermi Surface: Anomalous Hall Effect as a Topological Fermi-Liquid Property. *Phys Rev Lett* *93*, 206602. <https://doi.org/10.1103/PhysRevLett.93.206602>.
33. König, M., Wiedmann, S., Brüne, C., Roth, A., Buhmann, H., Molenkamp, L.W., Qi, X.-L., and Zhang, S.-C. (1980). Quantum Spin Hall Insulator State in HgTe Quantum Wells. *Science* (1979) *318*, 766–770.
34. Chang, C.-Z., Zhang, J., Feng, X., Shen, J., Zhang, Z., Guo, M., Li, K., Ou, Y., Wei, P., Wang, L.-L., et al. (2013). Experimental Observation of the Quantum Anomalous Hall Effect in a Magnetic Topological Insulator. *Science* (1979) *340*, 167–170.
35. Onoda, S., Sugimoto, N., and Nagaosa, N. (2008). Quantum transport theory of anomalous electric, thermoelectric, and thermal Hall effects in ferromagnets. *Phys Rev B* *77*, 165103. <https://doi.org/10.1103/physrevb.77.165103>.
36. Bergman, D.J., and Levy, O. (1991). Thermoelectric properties of a composite medium. *J Appl Phys* *70*, 6821–6833. <https://doi.org/10.1063/1.349830>.
37. Minor, W., Schonfeld, B., Lebech, B., Buras, B., and Dmowski, W. (1987). Crystallization of Fe-Si-B metallic glasses studied by X-ray synchrotron radiation. *J Mater Sci* *22*, 4144–4152.
38. McHenry, M.E., Johnson, F., Okumura, H., Ohkubo, T., Ramanan, V.R.V., and Laughlin, D.E. (2003). The kinetics of nanocrystallization and microstructural observations in FINEMET, NANOPERM and HITPERM nanocomposite magnetic materials. *Scr Mater* *48*, 881–887. [https://doi.org/10.1016/S1359-6462\(02\)00597-3](https://doi.org/10.1016/S1359-6462(02)00597-3).
39. Zhang, Y.R., and Ramanujan, R. V. (2005). The effect of niobium alloying additions on the crystallization of a Fe-Si-B-Nb alloy. *J Alloys Compd* *403*, 197–205. <https://doi.org/10.1016/j.jallcom.2005.05.019>.
40. Kim, S.G., Lee, N.E., and Ra, H.Y. (1988). Dendritic growth of a(Fe,Si) ferrite in annealed Fe₈₀Si₈B₁₂ metallic glass. *J Cryst Growth* *92*, 629–638.
41. Zhou, W., Miura, A., Sakuraba, Y., and Uchida, K.I. (2023). Direct Electrical Probing of Anomalous Nernst Conductivity. *Phys Rev Appl* *19*, 064079. <https://doi.org/10.1103/PhysRevApplied.19.064079>.
42. Miyasato, T., Abe, N., Fujii, T., Asamitsu, A., Onoda, S., Onose, Y., Nagaosa, N., and Tokura, Y. (2007). Crossover behavior of the anomalous Hall effect and anomalous Nernst effect in itinerant ferromagnets. *Phys Rev Lett* *99*, 086602. <https://doi.org/10.1103/PhysRevLett.99.086602>.
43. Xiao, D., Yao, Y., Fang, Z., and Niu, Q. (2006). Berry-phase effect in anomalous thermoelectric transport. *Phys Rev Lett* *97*, 026603. <https://doi.org/10.1103/PhysRevLett.97.026603>.
44. Guin, S.N., Manna, K., Noky, J., Watzman, S.J., Fu, C., Kumar, N., Schnelle, W., Shekhar, C., Sun, Y., Gooth, J., et al. (2019). Anomalous Nernst effect beyond the magnetization scaling relation in the ferromagnetic Heusler compound Co₂MnGa. *NPG Asia Mater* *11*, 16. <https://doi.org/10.1038/s41427-019-0116-z>.
45. Xu, L., Li, X., Ding, L., Chen, T., Sakai, A., Fauqué, B., Nakatsuji, S., Zhu, Z., and Behnia, K. (2020). Anomalous transverse response of Co₂MnGa and universality of the room-temperature $\alpha_{ij}A / \sigma_{ij}A$ ratio across topological magnets. *Phys Rev B* *101*, 180404(R). <https://doi.org/10.1103/PhysRevB.101.180404>.
46. Karplus, R., and Luttinger, J.M. (1954). Hall Effect in Ferromagnetics. *Physics Review* *95*, 1154–1160.
47. Hebel, L.C., and Smith, G.E. (1958). Interband transitions and band structure of a BiSb alloy. *Physics Letters* *10*, 273–275.
48. Gautam, R., Hirai, T., Alasli, A., Nagano, H., Ohkubo, T., Uchida, K., and Sepelri-Amin, H. (2024). Creation of flexible spin-caloritronic material with giant transverse thermoelectric conversion by nanostructure engineering. *Nat Commun* *15*, 2184. <https://doi.org/10.1038/s41467-024-46475-6>.
49. Medina, J., Green, D., and Chamon, C. (2013). Networks of quantum wire junctions: A system with quantized integer Hall resistance without vanishing longitudinal resistivity. *Phys Rev B Condens Matter Mater Phys* *87*, 045128. <https://doi.org/10.1103/PHYSREVB.87.045128/FIGURES/7/MEDIUM>.
50. Lee, J.M., Oshikawa, M., and Cho, G.Y. (2021). Non-Fermi Liquids in Conducting Two-Dimensional Networks. *Phys Rev Lett* *126*, 186601. <https://doi.org/10.1103/PHYSREVLETT.126.186601/FIGURES/2/MEDIUM>.

51. Bang, K.M., Park, S.J., Yu, H., and Jin, H. (2024). Large transverse thermopower in shape-engineered tilted leg thermopile. *Appl Energy* 368, 123222. <https://doi.org/10.1016/j.apenergy.2024.123222>.

Supplemental information for

Electron transverse transport enhancement by composite formation

Sang J. Park^{1,3,4}, Hojun Lee^{2,3}, Jongjun M. Lee², Jangwoo Ha¹, Hyun-Woo Lee^{2*} and Hyungyu Jin^{1,5*}

¹Department of Mechanical Engineering, Pohang University of Science and Technology (POSTECH), Pohang, 37673, South Korea.

²Department of Physics, Pohang University of Science and Technology (POSTECH), Pohang, 37673, South Korea.

³These authors contributed equally.

⁴Present address: National Institute for Materials Science, Tsukuba, 305-0047, Japan.

⁵Lead contact

*Correspondence: hgjin@postech.ac.kr (H.J.); hwl@postech.ac.kr (H.-W.L)

Table of contents

Supplemental Notes (S1-S6)

- 1. Network size dependence of the transverse conductivity**
- 2. Effect of geometric structures of domains on current path**
- 3. Effect of domain control on longitudinal electrical transport**
- 4. Effect of domain control on thermal conductivity**
- 5. Ratio of anomalous Nernst conductivity and anomalous Hall conductivity**
- 6. Contribution of the Seebeck-driven transverse voltage**

Supplemental Figures (Figs. S1-S13)

References (1-30)

In the main text, we theoretically proposed the enhancement of transverse transport (TT) based on the physical mixture and showed experimental evidence of enhanced TT in a heterostructure. Here, in Supplementary Materials, we provide additional theoretical and experimental information. Especially, we provide experimental evidence reinforcing the theoretical prediction that the enhanced TT originates from an extrinsic mechanism (*i.e.*, the wiggly path of electrons in the hetero-domain structures), not from intrinsic mechanisms. We do this by analyzing the ratio of anomalous Nernst conductivity (α_{yx}) and anomalous Hall conductivity (σ_{yx}), and investigating possible contribution of the Seebeck-driven transverse thermoelectric generation (STTG) to the observed anomalous Nernst coefficient (S_{yx}). Additionally, the effect of domain control on longitudinal electrical transport, including the residual resistivity ratio (RRR), Kondo-like resistivity upturns, and magnetoresistance (MR), is analyzed and discussed.

Note S1. Network size dependence of the transverse conductivity

We evaluate the network size dependence of the transverse conductivity γ_T , which is presented in Fig. 1b in the main text. The average $\bar{\gamma}_T$ of γ_T over 10 random arrangements (instead of 100) as a function of the portion of material B ($P^{(B)}$) for each N_x and N_y are presented in Fig. S1c to S1f. The junction parameters were set to be the same as those used for the result in Fig. 1b in the main text. $\bar{\gamma}_T$ (red symbols) is almost independent of the size of the network. These results are consistent with the fact that conductivity is an intrinsic property, which is independent of the system size. The deviation (red shaded area) increases as N decreases, which slightly increases $\bar{\gamma}_T$ as N decreases. This is because the current paths and the arrangement of possible geometric structures of domains are restricted as the network size decreases.

Note S2. Effect of geometric structures of domains on current path

To show that the geometric structure of physical domains generates the wiggly current paths, we investigate the current and potential distribution of the island structures (inset in Fig. 1b in the main text and Fig. S2). First, we consider the island structure in which the material A (amorphous, yellow) islands are embedded in the material B (crystalline, cyan) (Fig. S2A). If there is no physical mixture, the macroscopic potential distribution is linear, and the direction of its gradient is entirely determined by the ratio of longitudinal and transverse conductivity. However, the presence of islands distorts the macroscopic potential distribution, which causes the wiggly current paths (Fig. S2B). The current tends to flow along the material B region, avoiding the material A islands (red arrows in Fig. S2b and S2c). To show this more clearly, we obtain the current flowing in each junction of the A1 site (Fig. S2a, green circle) and the B1 site (Fig. S2a, red circle) from the potential distribution. The longitudinal current strength ($|I_3 - I_1|$) flowing the B1 site is 25.04, which is 12.13 times larger than the longitudinal current flowing the A1 site. The ratio of the transverse current strength ($|I_4 - I_2|$) to the longitudinal current strength is 0.60 at the B1 site, which is 5.04 times smaller than the ratio at the A1 site. We also calculate $(V - \mathcal{T}(V))/2$ to evaluate the transverse potential asymmetry (Fig. S2c), where V is the potential and \mathcal{T} is the time-reversal operator. The presence of the island locally enhances the asymmetry of the transverse potential, which implies an imbalance in the current deflected by the island. These results are consistent with our analysis in the main text. Next, we consider the island structure in which the material B islands are embedded in the material A (Fig. S2d). In this case, the current tends to minimize the portion in material A (Fig. S2e and S2f), which still leads to wiggly current paths.

Note S3. Effect of domain control on longitudinal electrical transport

First, we confirm that the controlled domain with varying annealing temperature (T_a) affects the longitudinal electrical transport. The electrical resistivity (ρ_{xx}) of the as-cast sample was $121 \mu\Omega\cdot\text{cm}$ at $T = 300 \text{ K}$. Intriguingly, annealing at $T_a = 673, 698 \text{ K}$ increased ρ_{xx} to $131\text{--}142 \mu\Omega\cdot\text{cm}$ (Fig. 3b in the main text), which can be attributed to the evolutions of local inhomogeneity and the (chemical) short-range order¹. This implies that the degree of disorder that free carriers experience within the solid is more pronounced in heterostructure samples than in a fully amorphous solid (as-cast), which is consistent with observations in multi-element complex alloys²⁻⁴. Subsequently, ρ_{xx} decreased to a saturated value ($\sim 60 \mu\Omega\cdot\text{cm}$) in crystalline samples with high T_a at 773 and 973 K .

The ρ_{xx} for all the samples exhibited a typical T -dependence of metals, where ρ_{xx} decreased with decreasing T (Fig. S6a). As electrons in metals mostly scatter with impurities at low temperatures rather than with phonons, RRR ($= \rho_{xx}(300 \text{ K})/\rho_{xx0}$, where ρ_{xx0} is the residual resistivity owing to the static impurities at low temperatures, here at $T=2 \text{ K}$) reflects the level of disorder in the samples. The amorphous samples exhibited a weak T dependence on ρ_{xx} with a small RRR of 1.04 compared with the crystallized $T_a=973 \text{ K}$ sample with an RRR of 2.08 (Fig. S9c). This demonstrates the strong localization of electrons by the disorder in amorphous samples. We note that the RRR value of the $T_a=973 \text{ K}$ sample is still smaller than that of Fe single- and polycrystalline samples (RRR of $\sim 7\text{--}86$)⁵, indicating existing structural or chemical disorders, as observed in Fig. 2 in the main text. In the heterostructure samples, upturns in ρ_{xx} were observed below $10\text{--}20 \text{ K}$, followed by a logarithmic T dependence down to 2 K (Figs. S9e – S9g), indicative of unconventional scattering affecting mobile carriers at low temperatures. These mechanisms include the Kondo effect^{6,7} owing to electron coupling with localized spin impurities, weak localization (WL)–induced quantum interference of electrons^{8,9}, or electron–electron interaction^{9,10}, all of which indicate the presence of local disorders. Notably, this upturn became negligible in the relatively more crystalline samples annealed above 723 K (Fig. S9h and S9i).

WL and weak antilocalization (WAL) describe the destructive and constructive quantum interferences of electron waves around self-intersecting paths, leading to increases and decreases in the ρ_{xx} , respectively^{7,8,10}. Under a magnetic field, these self-intersecting effects are mitigated, resulting in the negative MR for WL and positive MR for WAL. Therefore, analyzing MR can provide the information on how the carriers are affected by disorders within solids. The domain-controlled samples show a crossover of MR at a high field regime ($> 3\text{T}$) from negative (in as-cast sample) to positive MR ($T_a=973\text{ K}$) at $T=2\text{ K}$ (Fig. S10), suggesting the transition from WL to WAL as T_a increases, consistent with the T -dependent data presented above.

Note S4. Effect of domain control on thermal conductivity

As ANE-based transverse thermoelectrics are attracting much attention nowadays^{11,13,15,17–19,22,24,26}, we further evaluated the thermal conductivities (κ) of our samples to see their potential for thermoelectric applications. The κ of as-cast and heterostructure samples at 300 K exhibits almost constant values around 11 W/(m·K) and shows an abrupt rise to 22 W/(m·K) when T_a reaches 773 K (Fig. S7). Such a rapid transition in κ can be explained by the amorphous-to-crystalline structural transition with increasing T_a , which is consistently observed in the lattice thermal conductivity (κ_{lat}) calculated from the Wiedemann-Franz law (Fig. S7). Our heterostructure samples demonstrate notably low κ_{lat} of 3.3–5.8 W/(m·K) ($T_a = 673$ – 723 K), contrary to single crystals known for substantial ANE, such as Co_2MnGa ($\kappa_{\text{lat}} \sim 22.8$ W/(m·K)²⁰), Fe_3Ga ($\kappa_{\text{lat}} \sim 10.4$ W/(m·K)¹⁷), and Fe-based Heusler compounds ($\kappa_{\text{lat}} \sim 9.4$ – 10.6 W/(m·K)²⁹) at 300 K. This is attributed to the absence of long-range lattice order, resulting in localized vibrational modes³⁰. Such low κ combined with competitive S_{yx} values make the heterostructure samples advantageous for transverse thermoelectric energy conversion, where they can achieve a high transverse figure-of-merit ($z_{\text{TT}}T = \frac{S_{yx}^2 \sigma_{yy}}{\kappa} T$) for power generation or a high heat flux sensitivity ($= S_{yx}/\kappa$) for heat sensing applications¹².

Note S5. Ratio of anomalous Nernst conductivity and anomalous Hall conductivity

Next, we discuss the microscopic origin of ANE by analyzing the ratio of α_{yx} and σ_{yx} , as proposed by Xu et al.¹⁴ According to the Berry curvature (Ω_z) description on TT, σ_{yx} and α_{yx} can be expressed as

$$\sigma_{xy} = \frac{e^2}{\hbar} \int_{BZ} \frac{d^3k}{(2\pi)^3} f(k) \Omega_B, \quad (\text{Eq. S1})$$

$$\alpha_{xy} = \frac{ek_B}{\hbar} \int_{BZ} \frac{d^3k}{(2\pi)^3} s(k) \Omega_B, \quad (\text{Eq. S2})$$

where $f(k)$ is the Fermi-Dirac distribution and $s(k) = -f(k) \ln f(k) - (1-f(k)) \ln(1-f(k))$ is the entropy density of electron gas. Given the distinct distribution functions for AHE and ANE, σ_{yx} is obtained by an integration of Ω_B for all the occupied bands below E_F , while α_{yx} is determined by Ω_B near E_F . Equations S1 and S2 can be rewritten^{14,16} with proper length parameters of the Fermi wavelength λ_F and the de Broglie thermal wavelength

$$\Lambda = \sqrt{\frac{\hbar^2}{2\pi m k_B T}}:$$

$$\sigma_{xy} \approx \frac{e^2}{\hbar} \frac{1}{c} \left\langle \frac{\Omega_B}{\lambda_F^2} \right\rangle, \quad (\text{Eq. S3})$$

$$\alpha_{xy} \approx \frac{ek_B}{\hbar} \frac{1}{c} \left\langle \frac{\Omega_B}{\Lambda^2} \right\rangle, \quad (\text{Eq. S4})$$

where m and c are the mass of the particle and the lattice parameter along the applied magnetic field, respectively. In a high T regime, where λ_F becomes comparable with Λ , the α_{yx}/σ_{yx} ratio approaches $k_B/e=86 \mu\text{V}/\text{K}$. This tendency of α_{yx}/σ_{yx} near 300 K has well explained the TT in topological materials, whose large TT originate from the intrinsic Berry curvature, such as Co_2MnGa ¹⁴. In contrast, YbMnBi_2 showed a large discrepancy of the ratio from k_B/e , which was explained by possible extrinsic contributions due to the

large SOC¹⁸. Despite the small SOC of our samples without heavy elements, amorphous and hetero-domain samples show discrepancies from k_B/e near 300 K, indicating significant role of extrinsic mechanism (Fig. S11). By contrast, the crystalline sample ($T_a=973$ K) shows an increasing trend of α_{yx}/σ_{yx} , indicating dominant intrinsic mechanism. In summary, the implication derived from this result is consistent with our other observations, including the resistivity upturn and crossover of MR, in that they all indicate a crucial role of extrinsic mechanism in our heterostructure samples. In addition, as previously discussed regarding the relation between ρ_{yx} and M , neither large S_{yx} nor α_{yx} are attributed to the change in M (Fig. S12), making a distinction from conventional ANE materials whose S_{yx} scales with M^{20} .

Note S6. Contribution of the Seebeck-driven transverse voltage

Lastly, we briefly discuss other possibility that may increase S_{yx} . The hetero-domain samples can be considered as a composite of amorphous and crystalline phases. In such a composite structure, the longitudinal Seebeck voltage in one material (*e.g.*, crystal) can contribute ANE through AHE in the other material (*e.g.*, amorphous), a phenomenon referred to as the Seebeck-driven thermoelectric generation (STTG)²¹. Given the substantial anomalous Hall angle ($\sim 6.5\%$) of the amorphous material (as-cast), the large S_{yx} would be attributed to STTG if the Seebeck coefficient (S_{xx}) of crystalline materials is sufficiently large. To quantify the contribution of STTG on enhanced S_{yx} , we perform a COMSOL simulation using a simplified composite model assuming spherical composites (Fig. S13 and Materials and Methods). Given small amount of B (2.5 at.%), we considered stable Fe- and Si-based crystalline phases, whose material properties were taken from literatures^{12,23,25,27,28}. Figure S13 shows that the STTG effect in our samples is small and even decreases the total S_{yx} when the amorphous host is mixed with Fe, Fe₃Si, Fe₂Si, and FeSi, possibly due to the opposite sign in S_{yx} or electrical shunting. When FeSi₂ forms the composite with the amorphous host, S_{yx} increase, but the effect is negligible (less than 0.03 $\mu\text{V/K}$ at the volume ratio of crystalline material (V_c) of 7%. Note that considering the small atomic portion of Si (5 at.%), the V_c of 7% is the maximum that FeSi₂ can form in the host. Thus, we conclude that the contribution of STTG to the observed enhanced TT in our heterostructure samples is negligibly small.

Supplemental Figures

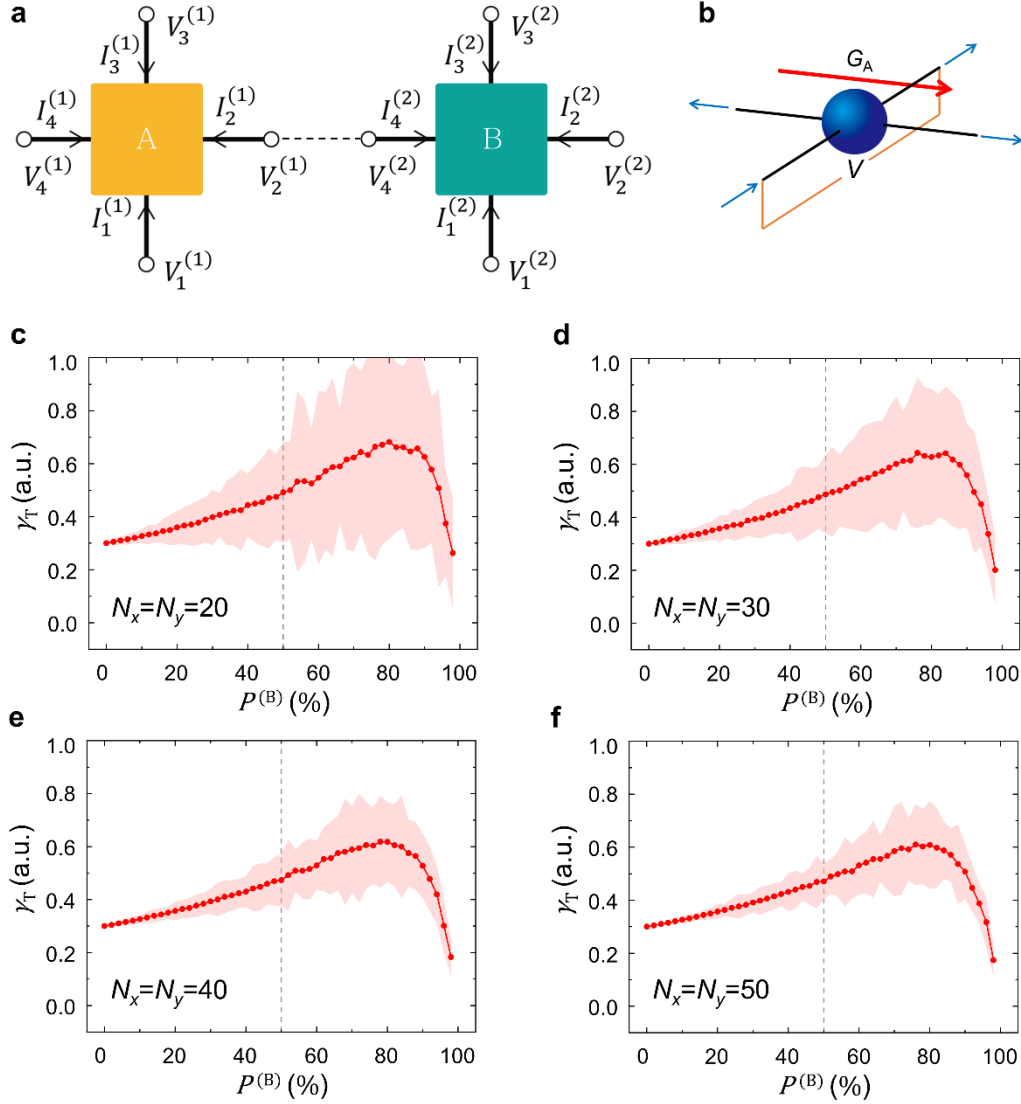


Fig. S1. Two-dimensional network model and network size dependence of the transverse conductivity. (a) Cross (+) junctions composing two-dimensional square network. Yellow and cyan squares represent material A (amorphous) and material B (crystalline), respectively. (b) Transverse current is characterized by the parameter G_A . (c to f) Transverse conductivity γ_T of random network for each network size N_x and N_y . The red symbols denote the average $\bar{\gamma}_T$ of γ_T over many random arrangements as a function of the portion of material B ($P^{(B)}$), whereas the red shaded area denotes 1.5- σ (standard deviation) range of γ_T .

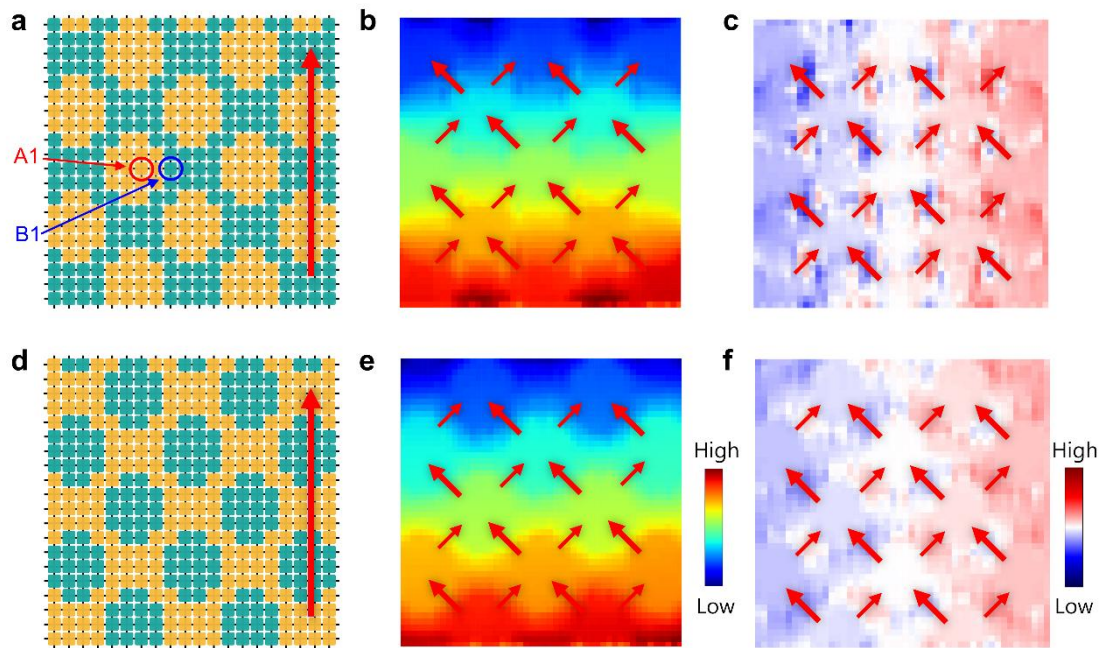


Fig. S2. Wiggly current paths originated from the geometric structures of domains. (a) Island structure in which material A (amorphous, yellow) islands are embedded in material B (crystalline, cyan). The red arrow represents a longitudinal flux. (d) Island structure in which material B islands are embedded in material A. (b and e) show potential distribution of the structure (a) and (b), respectively. (c and f) show transverse potential asymmetry of the structure a and b, respectively. The red arrows in (b to c) and (e to f) represent the current path distorted by the material A or B islands.

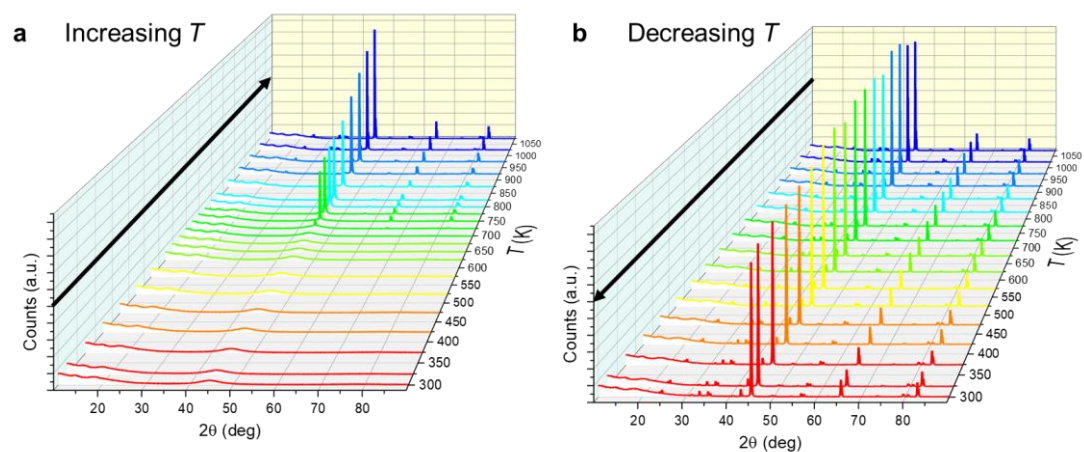


Fig. S3. In-situ X-ray diffraction patterns of the as-cast sample. In-situ X-ray diffraction patterns for (a) increasing temperature from 300 K to 1073 K and (b) decreasing from 1073 K to 300 K.

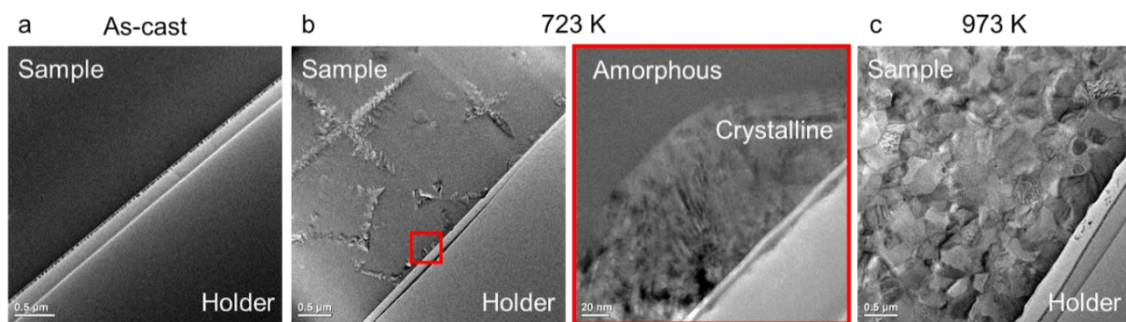


Fig. S4. Low magnification images of TEM samples. Images of (a), the as-cast sample, and samples annealed at (b), 723 K (hetero-domain) and (c), 973 K (fully crystallized).

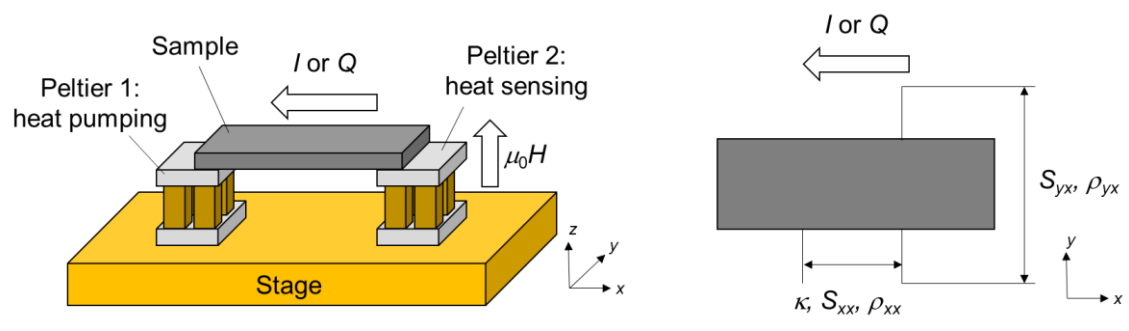


Fig. S5. Measurement configurations for electrical and thermal transport properties.

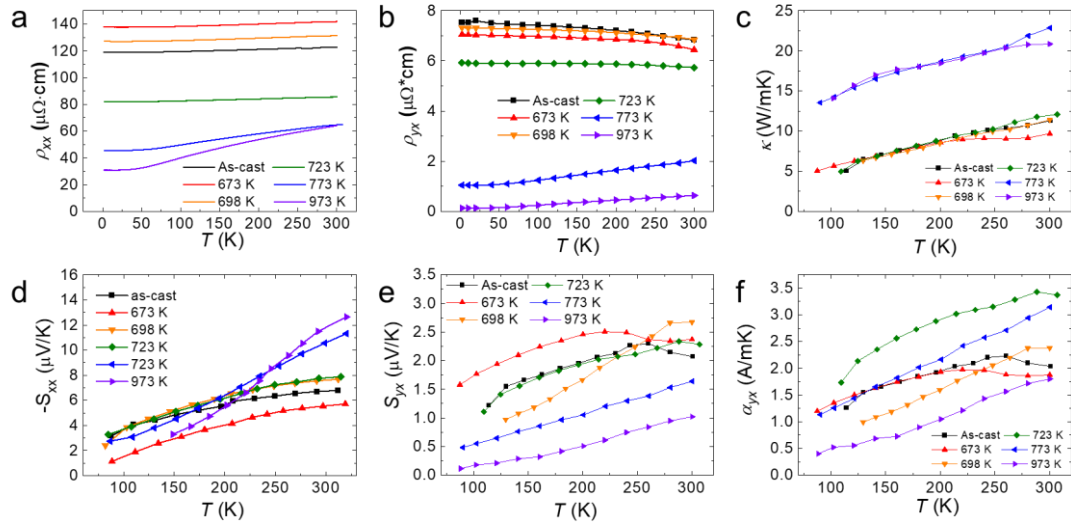


Fig. S6. Temperature dependent longitudinal and transverse transport properties. (a) electrical resistivity (ρ_{xx}), (b) anomalous Hall resistivity (ρ_{yx}), (c) thermal conductivity (κ), (d) Seebeck coefficient with negative sign ($-S_{xx}$), (e) anomalous Nernst coefficient (S_{yx}), and (f) anomalous Nernst conductivity (α_{yx}).

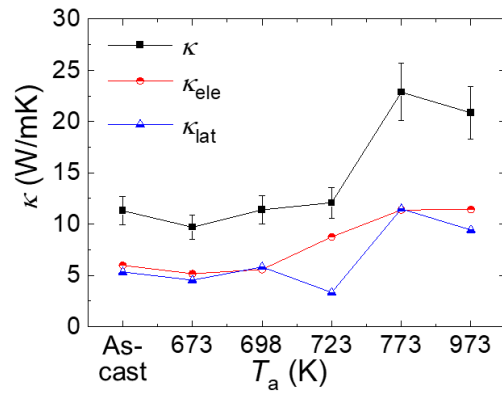


Fig. S7. Total (κ), electronic (κ_{ele}), and lattice (κ_{lat}) thermal conductivities of 1-hr annealed samples at room temperature.

$T_a=623, 673, 723, 773,$ and 823 K samples annealed for 5 min
 * $T_a = 973$ K sample annealed for 1 h

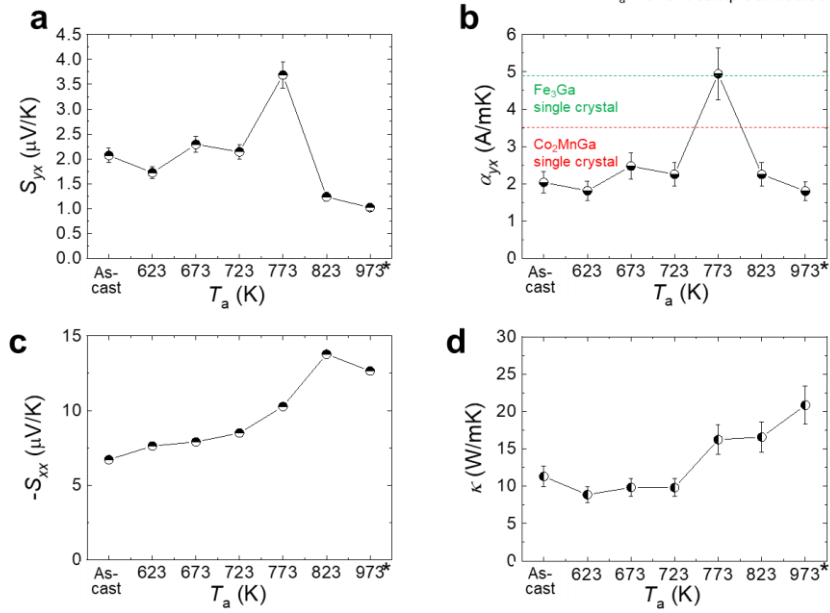


Fig. S8. Thermal transport properties in the sample set annealed for 5 min. (a) Anomalous Nernst coefficient (S_{yx}) and (b), anomalous Nernst conductivity (α_{yx}). The horizontal lines in (B) correspond to the values of Fe_3Ga and Co_2MnGa single crystals. (c) Longitudinal Seebeck coefficient with negative sign ($-S_{xx}$). (d) Longitudinal thermal conductivity (κ). All properties were measured at $T=300$ K. Note that data of the $T_a = 973$ K correspond to the sample annealed at $T_a = 973$ K for 1 h, served as the crystalline counterpart for comparison. The other data correspond to the samples annealed for 5 min aside from the as-cast sample.

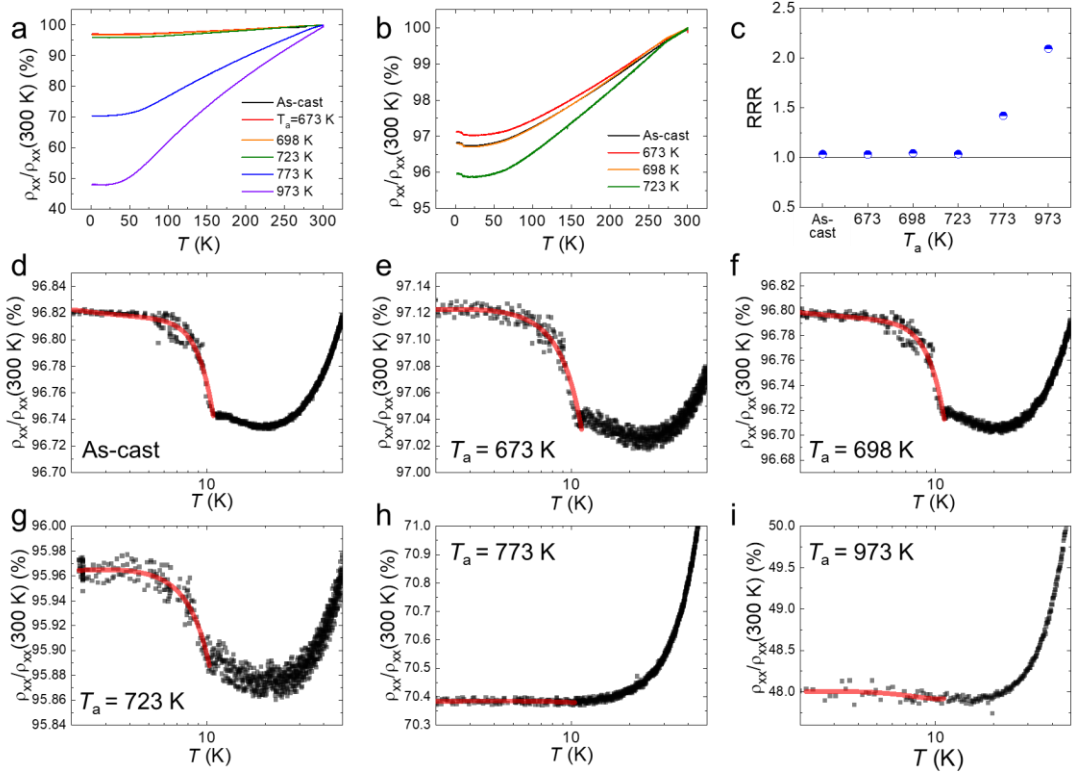


Fig. S9. Temperature dependent longitudinal electrical properties. (a and b) Electrical resistivity (ρ_{xx}) normalized by 300 K data $\rho_{xx}(300\text{ K})$ for all samples (a) and amorphous and hetero-domain samples (b). (c) Residual resistivity ratio (RRR = $\rho_{xx}(300\text{ K})/\rho_{xx}(2\text{ K})$). (d to i) $\rho_{xx}/\rho_{xx}(300\text{ K})$ at low temperature from 2 K to 50 K in as-cast (d), samples annealed at 673 K (e), 698 K (f), 723 K (g), 773 K (h), and 973 K (i). The red lines are the log functions for fitting. The resistivity upturns in amorphous and hetero-domain samples indicate the Kondo-like effects, including the Kondo effect, electron-electron interaction, and weak (anti)localization.

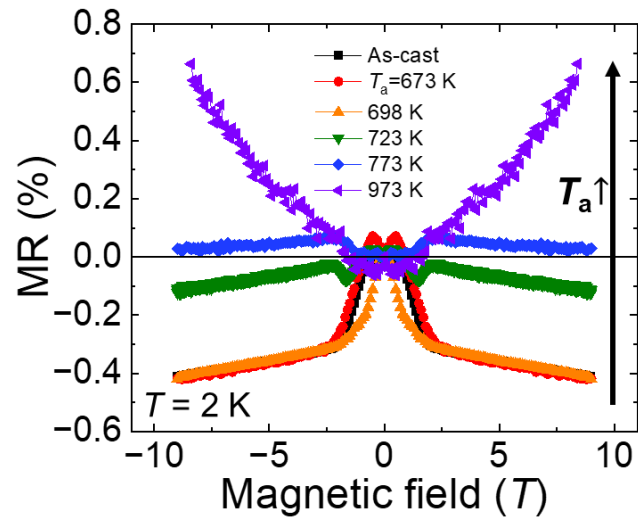


Fig. S10. Magnetoconductance (MR) at $T = 2$ K. The MR data show a transition from negative MR to positive MR with increasing T_a , which indicates a crossover of quantum interference of electron waves from weak localization to weak antilocalization.

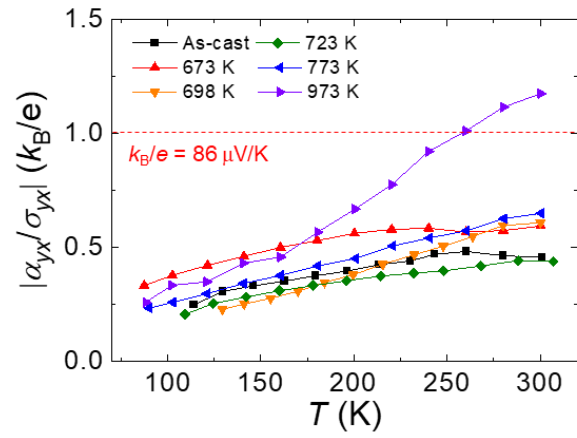


Fig. S11. Ratio of anomalous Nernst conductivity and anomalous Hall conductivity.

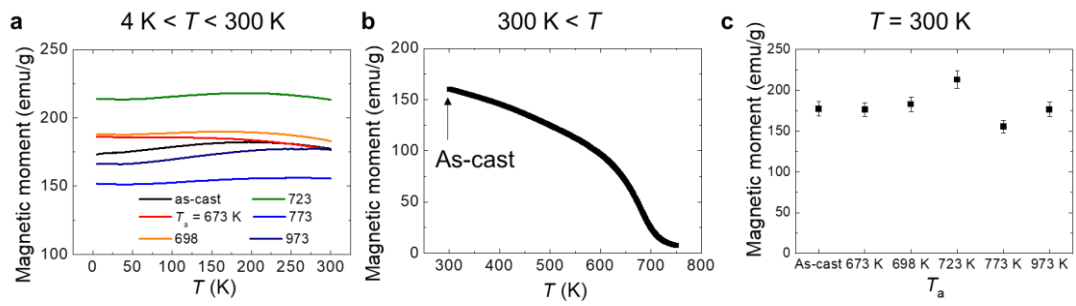


Fig. S12. Magnetic properties measured by VSM. Temperature dependent magnetic moments of the samples ranging (a), from 4 K to 300 K, and (b), from 300 K to 750 K. Note that the crystallinity of as-cast sample changes during the high-temperature measurement in (a). (c) Magnetic moments of the samples at 300 K.

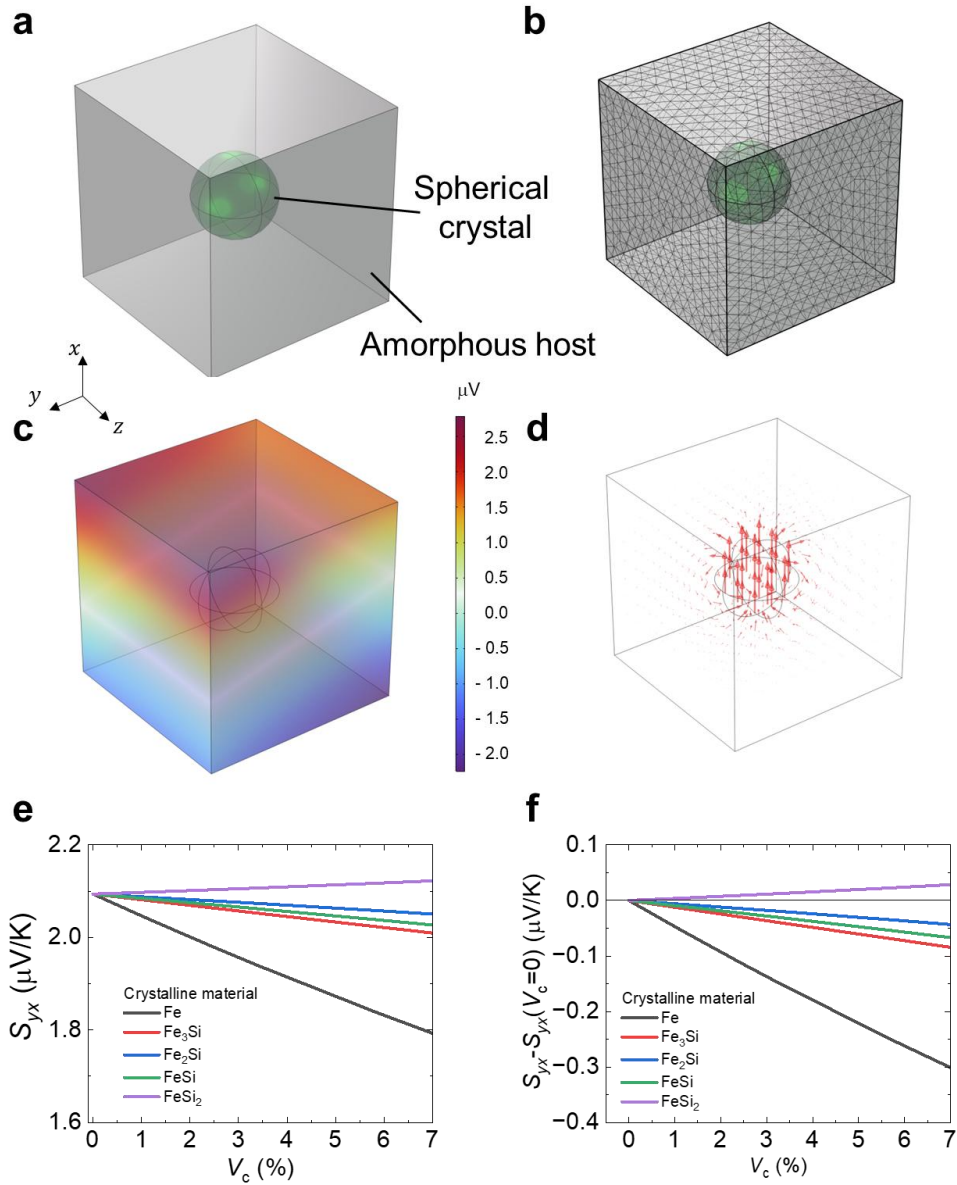


Fig. S13. Investigation of the possible contribution of Seebeck-driven transverse thermoelectric generation (STTG). (a) Simplified composite model used in this simulation, assuming spherical crystal in amorphous host. (b) Constructed mesh for finite element method. (c and d) Simulated voltage distribution in the composite. (e) Anomalous Nernst coefficient (S_{yx}) considering the STTG effect as a function of crystalline volume (V_c) (f) Changes in S_{yx} of composite compared to the as-cast sample ($S_{yx}(V_c=0)$).

References

1. Zhou, S., Dong, B., Xiang, R., Zhang, G., Qin, J., and Bian, X. (2015). Influence of clusters in melt on the subsequent glass-formation and crystallization of Fe-Si-B metallic glasses. *Progress in Natural Science: Materials International* 25, 137–140. <https://doi.org/10.1016/j.pnsc.2015.02.002>.
2. Tanimoto, H., Hozumi, R., and Kawamura, M. (2022). Electrical resistivity and short-range order in rapid-quenched CrMnFeCoNi high-entropy alloy. *J Alloys Compd* 896, 163059. <https://doi.org/10.1016/j.jallcom.2021.163059>.
3. Li, L., Chen, Z., Kuroiwa, S., Ito, M., Yuge, K., Kishida, K., Tanimoto, H., Yu, Y., Inui, H., and George, E.P. (2023). Evolution of short-range order and its effects on the plastic deformation behavior of single crystals of the equiatomic Cr-Co-Ni medium-entropy alloy. *Acta Mater* 243, 118537. <https://doi.org/10.1016/j.actamat.2022.118537>.
4. Manzoor Rana, A., Faheem Khan, A., Abbas, A., and Ansari, M.I. (2003). Electrical resistivity behavior in Ni-25 at.% Cr alloy. *Mater Chem Phys* 80, 228–231.
5. Watzman, S.J., Duine, R.A., Tserkovnyak, Y., Boona, S.R., Jin, H., Prakash, A., Zheng, Y., and Heremans, J.P. (2016). Magnon-drag thermopower and Nernst coefficient in Fe, Co, and Ni. *Phys Rev B* 94, 144407. <https://doi.org/10.1103/PhysRevB.94.144407>.
6. Dobrosavljevic, V., Kirkpatrick, T.R., and Kotliar, G. (1992). Kondo Effect in Disordered Systems. *Phys Rev Lett* 69, 1113–1116.
7. Molinari, A., Balduini, F., Rocchino, L., Wawrzyńczak, R., Sousa, M., Bui, H., Lavoie, C., Stanic, V., Jordan-Sweet, J., Hopstaken, M., et al. (2023). Disorder-Induced Magnetotransport Anomalies in Amorphous and Textured Co_{1-x}Si_x Semimetal Thin Films. *ACS Appl Electron Mater* 5, 2624–2637. <https://doi.org/10.1021/acsaelm.3c00095>.
8. Li, X., Li, P., Hou, V.D.H., DC, M., Nien, C.H., Xue, F., Yi, D., Bi, C., Lee, C.M., Lin, S.J., et al. (2021). Large and robust charge-to-spin conversion in sputtered conductive WTex with disorder. *Matter* 4, 1639–1653. <https://doi.org/10.1016/j.matt.2021.02.016>.
9. Lu, H.Z., and Shen, S.Q. (2015). Weak antilocalization and localization in disordered and interacting Weyl semimetals. *Phys Rev B Condens Matter Phys* 92, 035203. <https://doi.org/10.1103/PhysRevB.92.035203>.
10. Lee, P.A., and Ramakrishnan, T. V (1985). Disordered electronic systems. *Rev Mod Phys* 57, 287–337.
11. Uchida, K., and Heremans, J.P. (2022). Thermoelectrics: From longitudinal to transverse. *Joule* 6, 2240–2245. <https://doi.org/10.1016/j.joule.2022.08.016>.
12. Zhou, W., and Sakuraba, Y. (2020). Heat flux sensing by anomalous Nernst effect in Fe-Al thin films on a flexible substrate. *Applied Physics Express* 13, 043001. <https://doi.org/10.35848/1882-0786/ab79fe>.
13. Boona, S.R., Jin, H., and Watzman, S. (2021). Transverse thermal energy conversion using spin and topological structures. *J Appl Phys* 130, 171101. <https://doi.org/10.1063/5.0062559>.
14. Xu, L., Li, X., Ding, L., Chen, T., Sakai, A., Fauqué, B., Nakatsuji, S., Zhu, Z., and Behnia, K. (2020). Anomalous transverse response of Co₂MnGa and universality of the room-temperature $\sigma_{ijA} / \sigma_{ij}$ ratio across topological magnets. *Phys Rev B* 101, 180404(R). <https://doi.org/10.1103/PhysRevB.101.180404>.
15. Ikhlas, M., Tomita, T., Koretsune, T., Suzuki, M.T., Nishio-Hamane, D., Arita, R., Otani, Y., and Nakatsuji, S. (2017). Large anomalous Nernst effect at room temperature in a chiral antiferromagnet. *Nat Phys* 13, 1085–1090. <https://doi.org/10.1038/nphys4181>.
16. Ding, L., Koo, J., Xu, L., Li, X., Lu, X., Zhao, L., Wang, Q., Yin, Q., Lei, H., Yan, B., et al. (2019). Intrinsic Anomalous Nernst Effect Amplified by Disorder in a Half-Metallic Semimetal. *Phys Rev X* 9, 41061. <https://doi.org/10.1103/PhysRevX.9.041061>.
17. Sakai, A., Minami, S., Koretsune, T., Chen, T., Higo, T., Wang, Y., Nomoto, T., Hirayama, M., Miwa, S., Nishio-Hamane, D., et al. (2020). Iron-based binary ferromagnets for transverse thermoelectric conversion. *Nature* 581, 53–57. <https://doi.org/10.1038/s41586-020-2230-z>.
18. Pan, Y., Le, C., He, B., Watzman, S.J., Yao, M., Gooth, J., Heremans, J.P., Sun, Y., and Felser, C. (2022). Giant anomalous Nernst signal in the antiferromagnet YbMnBi₂. *Nat Mater* 21, 203–209. <https://doi.org/10.1038/s41563-021-01149-2>.
19. Sakai, A., Mizuta, Y.P., Nugroho, A.A., Sihombing, R., Koretsune, T., Suzuki, M.T., Takemori, N., Ishii, R., Nishio-Hamane, D., Arita, R., et al. (2018). Giant anomalous Nernst effect and

- quantum-critical scaling in a ferromagnetic semimetal. *Nat Phys* *14*, 1119–1124.
<https://doi.org/10.1038/s41567-018-0225-6>.
20. Guin, S.N., Manna, K., Noky, J., Watzman, S.J., Fu, C., Kumar, N., Schnelle, W., Shekhar, C., Sun, Y., Gooth, J., et al. (2019). Anomalous Nernst effect beyond the magnetization scaling relation in the ferromagnetic Heusler compound Co₂MnGa. *NPG Asia Mater* *11*, 16.
<https://doi.org/10.1038/s41427-019-0116-z>.
 21. Zhou, W., Yamamoto, K., Miura, A., Iguchi, R., Miura, Y., Uchida, K., and Sakuraba, Y. (2021). Seebeck-driven transverse thermoelectric generation. *Nat Mater* *20*, 463–467.
<https://doi.org/10.1038/s41563-020-00884-2>.
 22. He, B., Şahin, C., Boona, S.R., Sales, B.C., Pan, Y., Felser, C., Flatté, M.E., and Heremans, J.P. (2021). Large magnon-induced anomalous Nernst conductivity in single-crystal MnBi. *Joule* *5*, 3057–3067. <https://doi.org/10.1016/j.joule.2021.08.007>.
 23. Secco, R.A. (2017). Thermal conductivity and Seebeck coefficient of Fe and Fe-Si alloys: Implications for variable Lorenz number. *Physics of the Earth and Planetary Interiors* *265*, 23–34.
<https://doi.org/10.1016/j.pepi.2017.01.005>.
 24. Fu, C., Guin, S.N., Watzman, S.J., Li, G., Liu, E., Kumar, N., Süb, V., Schnelle, W., Auffermann, G., Shekhar, C., et al. (2018). Large Nernst power factor over a broad temperature range in polycrystalline Weyl semimetal NbP. *Energy Environ Sci* *11*, 2813–2820.
<https://doi.org/10.1039/c8ee02077a>.
 25. Hsin, C.L., Liu, Y.T., and Tsai, Y.Y. (2017). Suppressed Umklapp scattering of β -FeSi₂ thin film and single crystalline nanowires. *Nanotechnology* *28*, 485702. <https://doi.org/10.1088/1361-6528/aa904a>.
 26. Guin, S.N., Vir, P., Zhang, Y., Kumar, N., Watzman, S.J., Fu, C., Liu, E., Manna, K., Schnelle, W., Gooth, J., et al. (2019). Zero-Field Nernst Effect in a Ferromagnetic Kagome-Lattice Weyl-Semimetal Co₃Sn₂S₂. *Advanced Materials* *31*, 1806622.
<https://doi.org/10.1002/adma.201806622>.
 27. Buschinger, B., Geibel, C., Steglich, F., Mandrus, D., Young, D., Sarrao, J.L., and Fisk, Z. (1997). Transport properties of FeSi. *Physica B* *230–232*, 784–786.
 28. Hamada, Y., Kurokawa, Y., Yamauchi, T., Hanamoto, H., and Yuasa, H. (2021). Anomalous Nernst effect in Fe-Si alloy films. *Appl Phys Lett* *119*, 152404.
<https://doi.org/10.1063/5.0062637>.
 29. Mende, F., Noky, J., Guin, S.N., Fecher, G.H., Manna, K., Adler, P., Schnelle, W., Sun, Y., Fu, C., and Felser, C. (2021). Large Anomalous Hall and Nernst Effects in High Curie-Temperature Iron-Based Heusler Compounds. *Advanced Science* *8*, 2100782.
<https://doi.org/10.1002/advs.202100782>.
 30. Zhou, W.X., Cheng, Y., Chen, K.Q., Xie, G., Wang, T., and Zhang, G. (2020). Thermal Conductivity of Amorphous Materials. *Adv Funct Mater* *30*, 1903829.
<https://doi.org/10.1002/adfm.201903829>.